Recovery Act: Web-based CO_2 Subsurface Modeling

Final Scientific/Technical Report

Reporting Period: October 1, 2009 to December 31, 2012

Christopher Paolini and Jose Castillo

March 23, 2013

DOE Award Number DE-FE0002069

San Diego State University
5500 Campanile Drive
San Diego, CA 92182

Abstract – The Web-based CO_2 Subsurface Modeling project focused primarily on extending an existing text-only, command-line driven, isothermal and isobaric, geochemical reaction-transport simulation code, developed and donated by Sienna Geodynamics, into an easier-to-use Web-based application for simulating long-term storage of CO_2 in geologic reservoirs. The Web-based interface developed through this project, publically accessible via URL http://symc.sdsu.edu/, enables rapid prototyping of CO_2 injection scenarios and allows students without advanced knowledge of geochemistry to setup a typical sequestration scenario, invoke a simulation, analyze results, and then vary one or more problem parameters and quickly re-run a simulation to answer *what-if* questions. symc.sdsu.edu has 2x12 core AMD Opteron™ 6174 2.20GHz processors and 16GB RAM. The Web-based application was used to develop a new computational science course at San Diego State University, *COMP 670: Numerical Simulation of CO_2 Sequestration*, which was taught during the fall semester of 2012. The purpose of the class was to introduce graduate students to Carbon Capture, Use and Storage (CCUS) through numerical modeling and simulation, and to teach students how to interpret simulation results to make predictions about long-term CO_2 storage capacity in deep brine reservoirs. In addition to the training and education component of the project, significant software development efforts took place. Two computational science doctoral and one geological science masters student, under the direction of the PIs, extended the original code developed by Sienna Geodynamics, named *Sym.8*. New capabilities were added to Sym.8 to simulate non-isothermal and non-isobaric flows of charged aqueous solutes in porous media, in addition to incorporating HPC support into the code for execution on many-core XSEDE clusters. A successful outcome of this project was the funding and training of three new computational science students and one geological science student in technologies relevant to carbon sequestration and problems involving flow in subsurface media. The three computational science students are currently finishing their doctorial studies on different aspects of modeling CO_2 sequestration, while the geological science student completed his master's thesis in modeling the thermal response of CO_2 injection in brine and, as a direct result of participation in this project, is now employed at ExxonMobil as a full-time staff geologist.

TABLE OF CONTENTS

EXECUTIVE SUMMARY

The steady accumulation of greenhouse gases resulting from the combustion of fossil fuels has led to an increase in solar radiation trapped between the atmosphere and the earth. This increased radiation raises the temperature of the earth's atmosphere and ocean systems. Many researchers believe that continuing increases in temperature will lead to catastrophic changes in weather conditions around the globe. With carbon dioxide (CO_2) being the most abundant greenhouse gas, many efforts are underway to reduce the level of CO_2 entering the atmosphere. One promising technology involves the sequestration of CO_2 in deep rock formations. CO_2 is first separated from flue gas expelled by coal-fired power plants. Flue gas normally contains 10% to 15% CO_2 by volume. The collected CO_2 is then compressed to a supercritical phase ($ScCO_2$) and injected into underground formations, such as exhausted gas reservoirs or deep brine aquifers. It is believed that CO_2 can remain permanently sequestered in such formations, depending on the chemical and mechanical characteristics of the underground resident water and rock constituents. Through a grant provided by the US Department of Energy's National Energy Technology Laboratory (NETL), researchers in the Computational Science Research Center (CSRC) at San Diego State University (SDSU) developed a novel new software system that gives scientists and students an ability to simulate the long-term chemical, structural, and seismic consequences of injected $ScCO_2$ in deep geologic water-rock systems. The novelty of this software lies in its intuitive Web-based user interface which is designed to allow students, without advanced knowledge of geochemistry, to setup a typical sequestration scenario, invoke a simulation, analyze results, and then vary one or more problem parameters and quickly re-run a simulation to answer *what-if* questions. Students can quickly and easily define a computational domain consisting of an arbitrary number of lithologies and brine water mixtures, select a number of predefined kinetic mechanisms that govern the aqueous reactions of nearly forty predefined minerals, specify the physical dimensions of the formation rock, specify the mixture properties of an aqueous injectant solution of CO_2 in water, and compute chemical reactivity, mass and heat transport, and rock stress and strain characteristics. The Web application, publically accessible via URL http://symc.sdsu.edu/, has been developed using an Asynchronous JavaScript and XML (AJAX) methodology which results in an application interface that looks and feels like a traditional desktop application, but runs entirely within a standard Web browser and requires no special installation or third-party browser plugins. This approach effectively maximizes the accessibility of our software to researchers, engineers, and students investigating carbon capture and sequestration processes. The Web-based application was used to create a new computational science course at San Diego State University, *COMP 670: Numerical Simulation of CO_2 Sequestration*, which was taught during the fall semester of 2012. The class introduced graduate students to Carbon Capture, Use and Storage (CCUS) through numerical modeling and simulation, and taught students how to interpret simulation results to make predictions about long-term CO_2 storage capacity in deep brine reservoirs. In addition to providing training opportunities for graduate students, a significant amount of software development has taken place over the last three years. Two computational science doctoral and one geological science masters student, under the direction of the PIs, extended a generalized water-rock

reaction-transport code developed by Sienna Geodynamics, named *Sym.8*. The existing code simulates aqueous chemical interaction between minerals and fluids under equilibrium (infinitely fast kinetics) conditions and kinetic rates. The code accounts for mineral precipitation and dissolution, which changes the formation porosity and permeability. New capabilities were added to Sym.8 to simulate non-isothermal and non-isobaric flows of charged aqueous solutes in porous media, in addition to incorporating HPC support into the code for execution on many-core XSEDE clusters. A successful outcome of this project was the funding and training of three new computational science students and one geological science student in technologies relevant to carbon sequestration and problems involving flow in subsurface media. The three computational science students are currently finishing their doctorial studies on different aspects of modeling CO_2 sequestration, while the geological science student completed his master's thesis in modeling the thermal response of CO_2 injection in brine and, as a direct result of participation in this project, is now employed at ExxonMobil as a full-time staff geologist. Over the three-year project period, the PIs and four students explored several research areas using the Web-based interface and extended Sym.8 code. The first effort focused on simulating short-term geochemical effects arising from the injection of CO_2-charged water in saline sedimentary basins, similar to the sandstone lithology of the Frio Formation, a regional brine and oil reservoir along the U.S. Gulf Coast. One-dimensional horizontal simulations were run with CO_2 aqueous concentrations of 0.5M being injected for 5 years at varying seepage velocities, with reservoir temperatures ranging from 20°C to 140°C. Simulation results showed a moving volume of water with a relatively high concentration of H^+ ion forms from the hydration of CO_2 that occurs when the injectant water mixes with the reservoir formation water. Results showed that the diffusion driven mass transport of H^+ throughout the reservoir sandstone occurs at a faster seepage velocity than the injectant water velocity or *sweep* velocity. Thus, when evaluating and monitoring CO_2 injection, it is important to consider the acidic front that can develop ahead of the CO_2 plume and its effects on reservoirs and seals. The second effort focused on the development of a numerical heat transfer module into Sym.8 to study temperature effects resulting from CO_2-rich injection into sedimentary basins. The temperature module iteratively calculates thermophysical properties of charged aqueous solutes and uses these properties to compute a spatial and temporal temperature profile. An advection-diffusion model governing heat transport is solved using a finite volume method with solute specific partial molal enthalpy and partial molal heat capacity values calculated using the Helgeson-Kirkham-Flowers (HKF) model. The temperature module has been used to study the thermal effects resulting from injection of CO_2-rich water into the Oligocene Frio Formation along the Texas Gulf Coast, with simulation parameters similar to the Frio Test Pilot Experiment. The third effort focused on the development of a poroelastic module to simulate rock fractures that develop as a result of internal stresses induced by the injection of CO_2-rich water. The pore-pressure module utilizes computed mean stresses and Oda's permeability tensor to calculate the impact of fractures on formation permeability. Fourth, we developed a new numerical scheme whereby all solute concentrations in all control volumes are solved simultaneously by constructing a large block-banded sparse matrix of rank $N_a \times N_x$, for N_a solutes and N_x control volumes, that is factored in a distributed-parallel fashion on many-core XSEDE clusters.

REPORT DETAILS

Experimental Methods

Web Interface Development

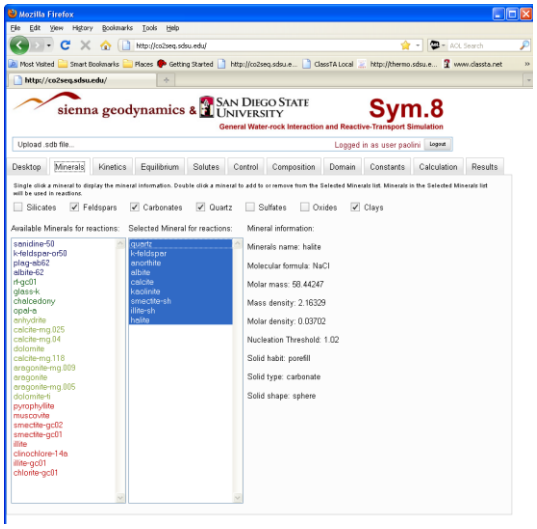

Figure 1. Defining a reservoir lithology using the Sym.8 Web interface developed through this project.

A Web-interface was developed to provide an easy-to-use interface to a generalized water-rock reaction-transport code developed by Sienna Geodynamics, named *Sym.8*. The novelty of this software lies in its intuitive Web-based user interface which is designed to allow students, without advanced knowledge of geochemistry, to setup a typical sequestration scenario, invoke a simulation, analyze results, and then vary one or more problem parameters and quickly re-run a simulation to answer *what-if* questions. Students can quickly and easily define a computational domain consisting of an arbitrary number of lithologies and brine water mixtures, select a number of predefined kinetic mechanisms that govern the aqueous reactions of nearly forty predefined minerals, specify the physical dimensions of the formation rock, specify the mixture properties of an aqueous injectant solution of CO_2 in water, and compute chemical reactivity, mass and heat transport, and rock stress and strain characteristics. The Web application ("Web-app"), publically accessible via URL http://symc.sdsu.edu/, has been developed using an Asynchronous JavaScript and XML (AJAX) methodology which results in an application interface that looks and feels like a traditional desktop application, but runs entirely within a standard Web browser and requires no special installation or third-party browser plugins. This approach effectively maximizes the accessibility of our software to researchers, engineers, and students investigating carbon capture and sequestration processes.

The Web application developed through this project was designed to allow students to investigate geochemical changes that occur when CO_2 rich water is injected into a brine water-sandstone rock system. The Web-app employs a left to right workflow paradigm where the minerals used in one or more lithologies are selected first, as shown in Figure 1. After mineral specification, the user then clicks on the *Kinetics* tab which will present the user with all atomically feasible "kinetic" (i.e. relatively slow) reactions, based on the minerals chosen in the *Minerals* tab, as shown in Figure 2. For each reaction, one can choose to use theoretical data by clicking the *Use Theoretical Reaction* button, or choose empirically derived kinetic reaction data by clicking the *Use Empirical Reaction* button. Selecting a reaction in the available reaction menu will show the forward reaction rate equation governing mineral dissolution, species governed by

the reaction, Arrhenius parameters (the pre-exponential factor *A* and activation energy E_a used to compute the "forward" dissolution rate constant k_f), and a polynomial expression used to compute the log of the concentration equilibrium constant K_c.

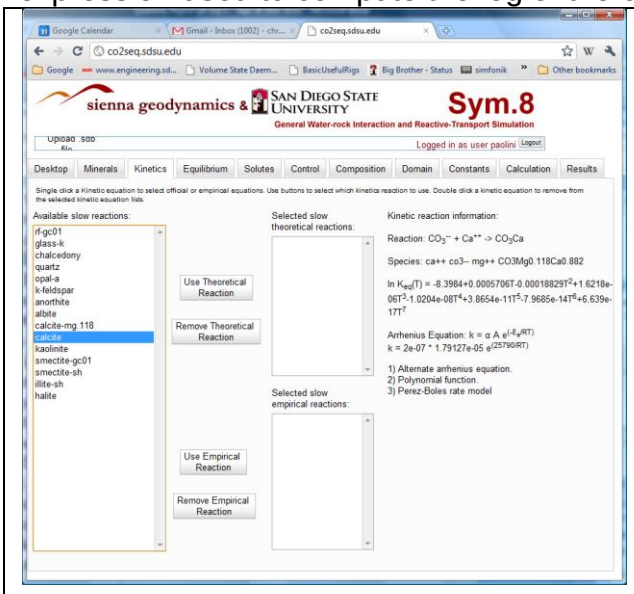

Figure 2. Selecting feasible "kinetic" (i.e. relatively slow) reactions that govern mineral dissolution or precipitation.

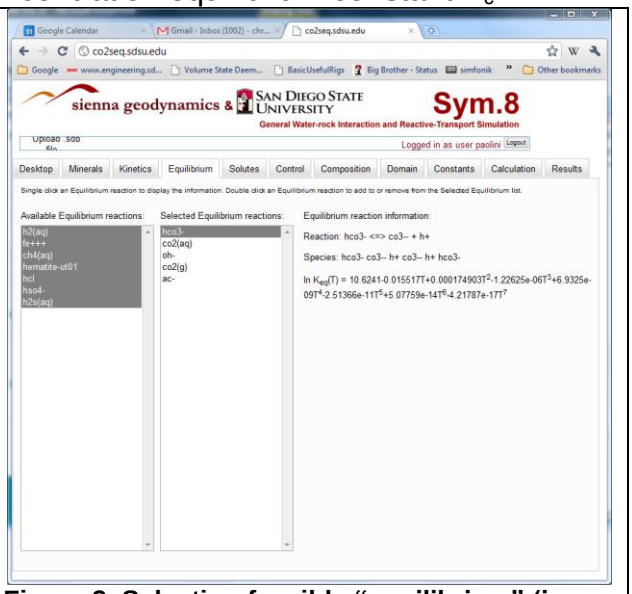

Figure 3. Selecting feasible "equilibrium" (i.e. relatively fast) reactions that govern solute dissolution or evolution.

After defining which kinetic reactions will be used in a simulation, one then moves to the *Equilibrium* tab and selects reactions that govern solute concentration. These reactions are called *equilibrium reactions* because they occur at much faster rates than mineral dissolution or precipitation reactions and hence reach an equilibrium state on a much faster time scale than "kinetic" reactions that involve the interaction of H_2O with rock. These equilibrium reactions involve the dissolution or evolution of solutes, as shown in Figure 4. In the *Solutes* tab, the Web-app lists the possible species that can exist in resident brine water as H2O reacts with rock.. After defining which equilibrium reactions will be used, the user proceeds to the right and clicks on the *Solutes* tab. In the *Solutes* tab, the Web-app lists the possible species that may exist at some time in the resident brine water as H_2O reacts with minerals in rock. A screenshot of the *Solutes* tab is shown in Figure 4. After viewing solute species, one moves to the *Control* tab, which allows a user to configure certain parameters that affect how a simulation will execute. These properties include such attributes as the system orientation, tortuosity model, and simulation time step values. A figure showing the *Control* tab is given in Figure 5. After configuring simulation control parameters, one moves to the *Composition* tab where the mixture properties of water solutions and rock lithologies are specified. Figure 6 shows a screen shot of the properties of a water mixture that is intended to represent formation water in sandstone. The composition of a water solution is defined by the concentration of solutes in the water by units of molarity, parts per million, pH, or pOH. The composition of a lithology is defined by the set of minerals that form the lithology along with each mineral's volume fraction and average grain radius. Next is the *Domain* tab where the physical characteristics of the reservoir are specified, as well as the characteristics of the numerical grid used to compute the species concentrations and

other conserved variables. Figure 7 shows a screen shot of the *Lithology* sub-tab in the *Domain* tab. In this image, a 100m long section of sandstone with 10 control volumes numerically representing a modeled reservoir is defined. The user can draw either a horizontal or a vertical depiction of one or more lithologies used in a given simulation. The graphical pallet shown in Figure 7 will list the order and type of lithologies selected for inclusion in a simulation. After specifying physical and numerical properties of the domain, the user clicks on the *Water Composition vs. Time* sub-tab and defines which

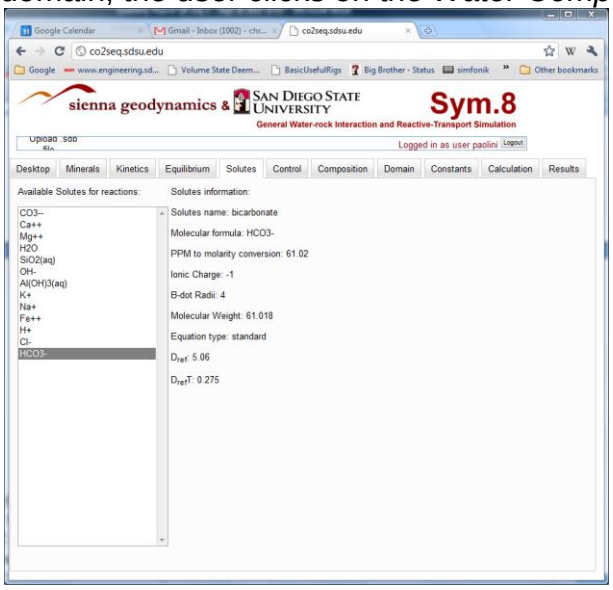

Figure 4. In the *Solutes* tab, the Web-app lists the possible species that can exist in resident brine water as H_2O reacts with rock.

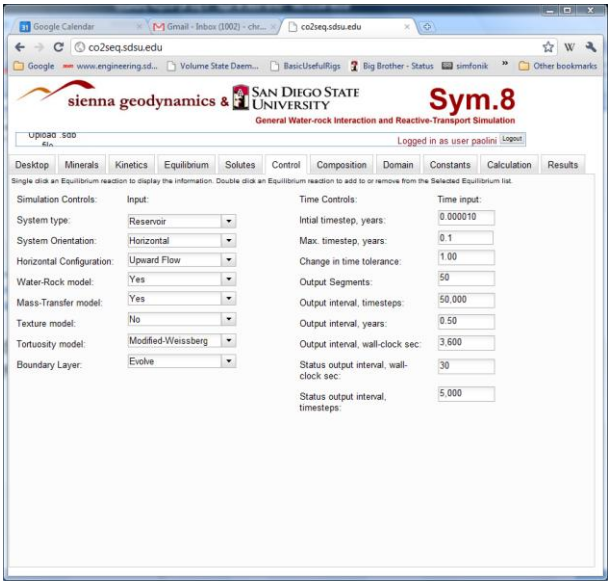

Figure 5. In the *Control* tab, one configures simulation specific parameters.

compositions will be used as injectants and which water composition will be used as the formation or resident water. This tab is shown in Figure 8. It is possible to define several different water compositions and return to this sub-tab and select a different injectant mixture in successive simulations. The *mybp* unit stands for *millions of years before present*. Using this parameter, one can simulate the injection of different water compositions at different times. Finally, to complete the domain specification, one clicks on the *Subsidence Configuration* tab as shown in Figure 9. Subsidence is the downward motion associated with sedimentation and tectonic movements. The flux parameter is the seepage velocity, which is the ratio of Darcy flux q and porosity φ. In this tab, one also can define the initial reservoir background temperature and surface temperature. The *Constants* tab shown in Figure 10 is used to specify the value of global variables used by the simulation subsystem that control textural and porosity models. For most studies, these parameters can be left with the given default values. The second to last tab is the *Calculation* tab shown in Figure 11. After configuring a problem, a user clicks the *Run Simulation* button in the *Calculation* tab. This button will invoke a new Java thread on the symc.sdsu.edu server that will launch and manage a simulation. One can enter an arbitrary note in the description field to identify a particular configuration. Since simulations can last hours or days, one can logout of the Web-app by clicking the *Logout* button in the upper menu bar and return some time later to check on the status of one or more long running simulations. Clicking on a row in the simulation table will allow one to manage a simulation. While a simulation is running,

the *Thread State* will be listed as *WAITING*. When a simulation has finished, the *Thread State* will be listed as *TERMINATED*. If a simulation terminates unexpectedly, one can view the simulation's log file to determine what went wrong by clicking on the respective row and selecting the *View Log* option. When a simulation terminates after running successfully, clicking on the respective row and selecting *View Results* will raise the *Results* tab and allow one to generate a superimposed plot of any number of variables with respect to space. Figure 12 shows an example of plotting the concentration of H^+ and Fe^{++}.

Course Development

The Web-based application developed through this project was used to create a new computational science course at San Diego State University, *COMP 670: Numerical Simulation of CO_2 Sequestration*, which was taught during the fall semester of 2012. The class introduced graduate students to Carbon Capture, Use and Storage (CCUS) through numerical modeling and simulation, and taught students how to interpret simulation results to make predictions about long-term CO_2 storage capacity in deep brine reservoirs. The topics covered in this course included: current Carbon Capture and Sequestration (CCS) technologies, how to configure and run a CCS problem using the Web-based CCS simulation application developed for the course, how to use the simulator to plot concentration, saturation, permeability, and porosity plots and interpret results, the thermodynamics of CO_2, Darcy's Law and flow through porous media, permeability and porosity, sedimentary rocks, the permeability and porosity of shale and sandstone, seepage velocity, mass and heat transport governing equations, kinetic reactions involving the dissolution and precipitation of minerals in shale and sandstone, advection and diffusion of solutes in aqueous systems, governing equations involving the conservation of mass, energy, and momentum, chemical equilibrium, numerical methods used to solve kinetic and equilibrium reactions governing water-rock interaction, analysis of a case study involving CO_2 injection in the Frio Formation at the South Liberty Oilfield, Enhanced Oil Recovery (EOR), the SACROC (Scurry Area Canyon Reef Operators Committee) Unit of the Kelly Snyder Field in Scurry County West Texas, the Bravo Dome in Colorado and McElmo Dome in New Mexico, CO_2 miscibility in oil and Minimum Miscibility Pressure (MMP) testing, wellbore design and engineering, blowout prevention devices, the chemistry of cements used to seal the annular volume between casing and borehole walls and the effect of CO_2 injection on Portland based cements, Coal Bed Methane (CBM) extraction, geologic formation of different types of coal, technologies used in CH_4 extraction, and Liesegang banding. In terms of learning outcomes, students gained a solid foundation of the fundamental thermodynamic and kinetic principles that govern geological CO_2 sequestration. Students gained a detailed understanding of the thermodynamic properties of carbon dioxide and carbon dioxide-water systems as well as the kinetics of mineral dissolution and precipitation reactions that govern silicates, feldspars, oxides, sulfates, clays, and carbonates.

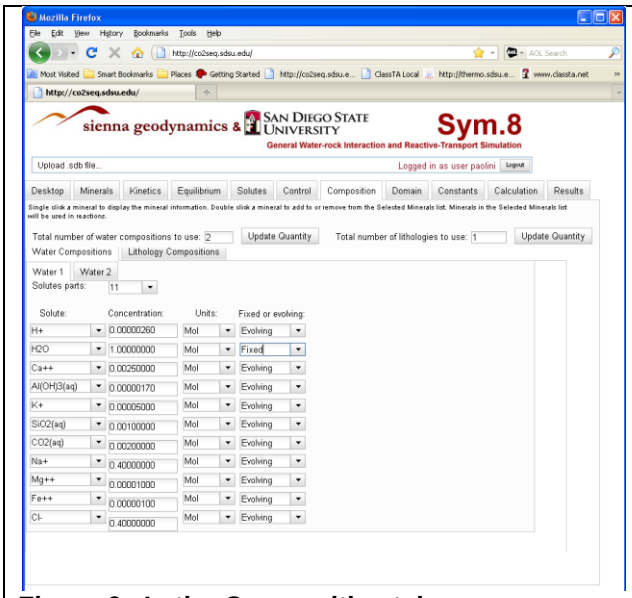

Figure 6. In the *Composition* tab one configures the mixture properties of resident and injectant waters, as well as one or more lithologies.

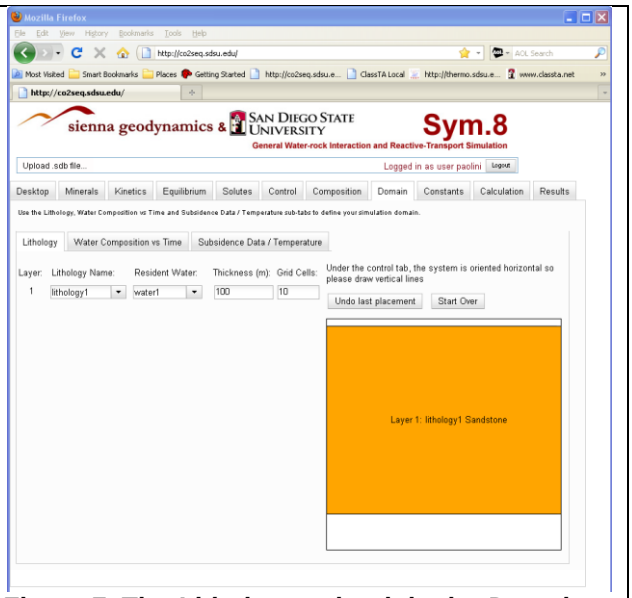

Figure 7. The *Lithology* sub-tab in the *Domain* tab defines the physical characteristics of the reservoir into which we will be injecting CO_2-rich H_2O. This tab also defines the numerical grid upon which the resulting system of PDEs will be solved.

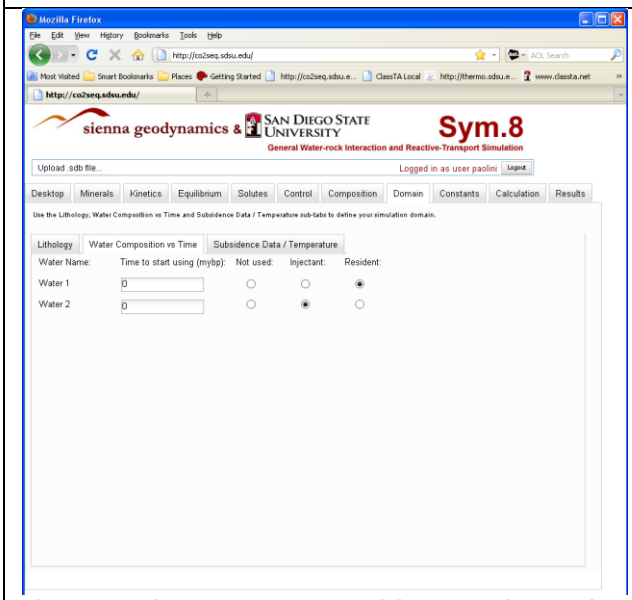

Figure 8. The Water Composition vs. Time sub-tab defines which water compositions will be used as injectant solutions and which water compositions will be used as the resident or formation water.

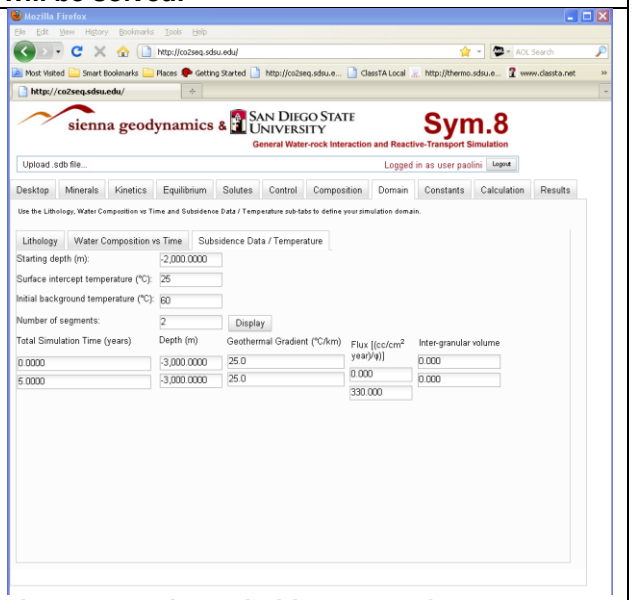

Figure 9. In the *Subsidence Data/Temperature* tab, one defines the time to start injecting different waters identified as injectants and their seepage velocity through the reservoir. In this tab, one also can define the initial reservoir background temperature and surface temperature.

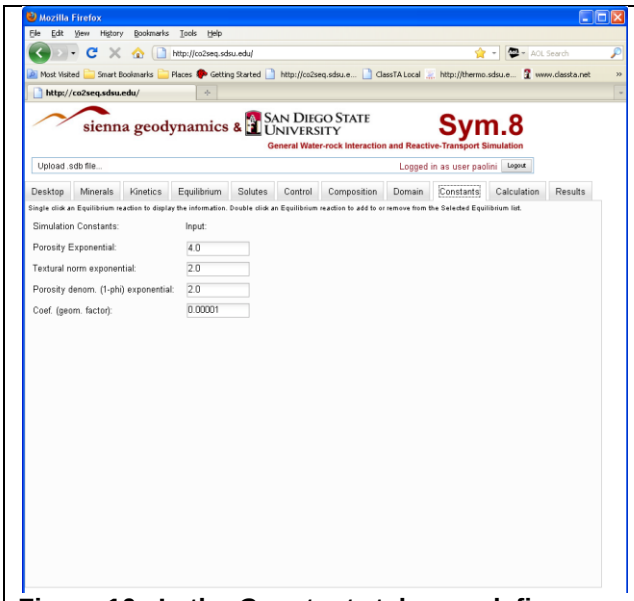

Figure 10. In the *Constants* tab, one defines global variables used by the simulation subsystem. For most studies, these parameters can be specified with the given default values.

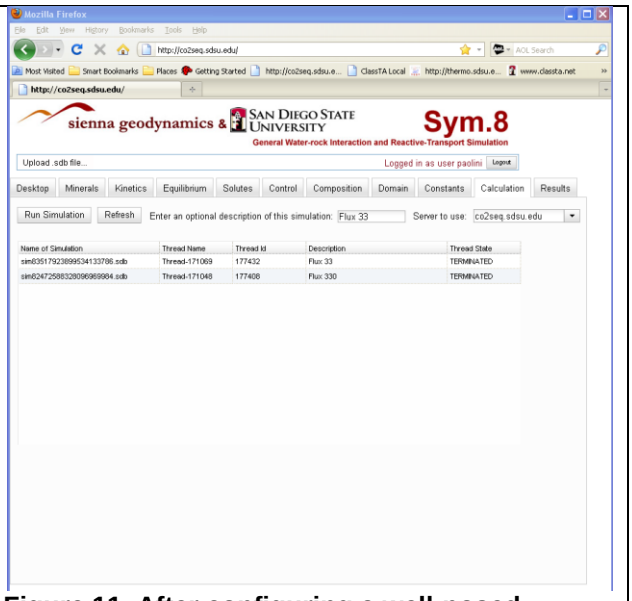

Figure 11. After configuring a well-posed problem, a user clicks the *Run Simulation* button in the *Calculation* tab. This button will invoke a new Java thread on the symc.sdsu.edu server that will launch and manage a simulation.

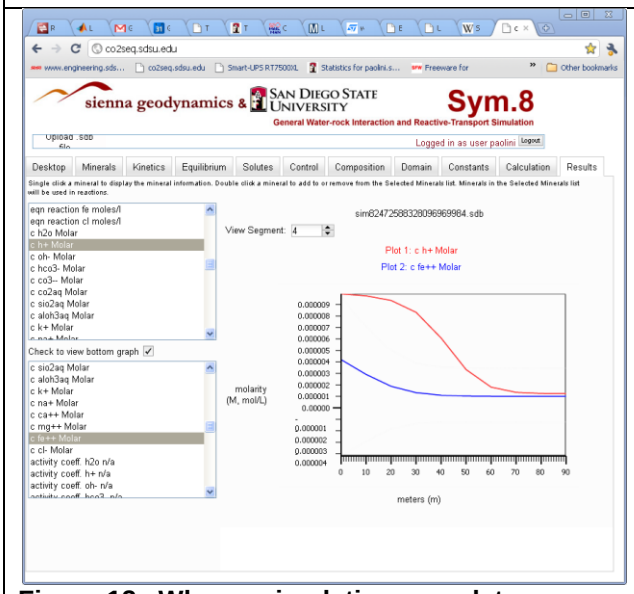

Figure 12. When a simulation completes successfully, clicking in the simulation table and selecting the *View Results* option will raise the *Results* tab and allow one to plot any number of variables with respect to space.

An outline of the primary topics discussed in the class are as follows:

1. Thermodynamics of carbon dioxide and carbon dioxide-water systems
    a. Chemical potentials
    b. Fugacity and activity
    c. Chemical equilibrium
    d. Gibbs free energy
    e. Phase diagrams
    f. Redlich-Kwong equation of state
    g. Peng-Robinson equation of state
2. Aqueous geochemistry
    a. Debye-Hückel theory
    b. Activity coefficients of ions
    c. The HKF and Pitzer models for properties of electrolyte solutions
3. Mineral chemistry
    a. Carbonate systems
    b. Silicas
    c. Clay minerals
    d. Gas-solid carbonation reactions
4. Mineral carbonation reaction kinetics
    a. Rate expressions and constants
    b. Reaction order
    c. Solving systems of ODEs using multi-step integration methods
    d. Transition state theory
    e. Mineral precipitation and dissolution reactions
    f. Dissolution and precipitation rates of silica minerals
    g. Dissolution rates of oxides
    h. Calcite kinetics
5. CO_2 sequestration simulation
    a. Introduction to WebSimC
    b. Darcy's law and flow through porous media
    c. Equations governing solute advection and diffusion
    d. Porosity and permeability
    e. Dynamic viscosity
    f. Seepage velocity
    g. Configuring formation and CO_2-rich injection water mixtures
    h. Lithology configuration
    i. Solute selection
    j. Subsidence configuration
    k. Running and analyzing CCS simulations using WebSimC
    l. Mass and energy transport
    m. Thermal diffusivity
    n. Generating and interpreting concentration profile plots
    o. Case study: CO_2 injection in the Frio Formation at the South Liberty Oilfield
6. Introduction to enhanced oil recovery

a. Oil extraction
b. Pipeline systems
c. Miscibility and Minimum Miscibility Pressure (MMP)
d. Miscible and immiscible displacements
e. Well design, well heads, Christmas trees, casings, and blowout preventers
f. Cements and cement chemistry

7. Introduction to coal bed methane (CBM) extraction
    a. Methane reactions
    b. Case studies: Powder River Basin and Tongue River Valley
    c. Environmental issues in CBM

The course began August 30, 2011, ended on December 15, 2011, and was taught on Tuesday and Thursday from 4:00 PM to 5:15 PM. Exams and coursework consisted of a series of problem sets where students wer required to solve, either manually or with the use of MATLAB, WebSimC, TOUGHREACT2, *EQ3/6,* and PHREEQC, short computational problems involving *aqueous* geochemistry with applications in CCS. The weights assigned to coursework components as percentages of the student's final grade were 35% for homework (problem sets), 20% midterm #1, 20% midterm #2, and 25% for the final exam. This class was classified as a three unit lecture course.

Students used the Web-based CCS simulation application developed for the course to solve "real-world" problems involving geochemical changes that occur when CO_2-rich water is injected into a brine water-sandstone rock system. One problem was to investigate the variation in the sweep and diffusion front displacement as a function of reservoir temperature and seepage velocity. The physical domain of this problem modeled the scenario conducted at the Frio Formation in 2004 and published in 2006 by Kharaka et al. [1] in which 1600 tons of CO_2 were injected at a depth of 1500m into a 24-m-thick sandstone section of a regional brine and oil reservoir in the U.S. Gulf Coast. Students investigated the potential for geologic storage of CO_2 in saline sedimentary aquifers by using the Web-app, where the rapid dissolution of calcite $CaCO_3$ and iron oxyhydroxides ($Fe(OH)_3$) caused by low pH conditions resulted from brine coming into contact with injected supercritical phase CO_2. Students studied how rapid mineral dissolution creates pathways in rock seals and well cements that can permit unwanted leakage of CO_2 and brine. Brine leakage containing dissolved toxic species (Fe, Mn) into an overlying drinking water supply poses a health hazard and mobilization of toxic organic compounds such as benzene and toluene poses an environmental hazard [1]. Using the Web-app, students also investigated the formation of a proton (H^+) diffusion front that forms ahead of a sweep front identified by a change in Fe^{++} ion concentration. A significant finding of the Frio Brine Pilot experiment was that injected CO_2 causes the brine at depth to become acidic. Acidic brine dissolves some of the rock and minerals it comes into contact with, adding iron and other metals to the salt water. Acidic brine can also allow the brine/CO_2 mixture to open new pathways through sandstone. In particular, the Frio experiment showed a pH decrease before the arrival of HCO_3^-, as

shown in Figure 13. Students were asked to show if a simulation showed the same result and to provide a possible explanation.

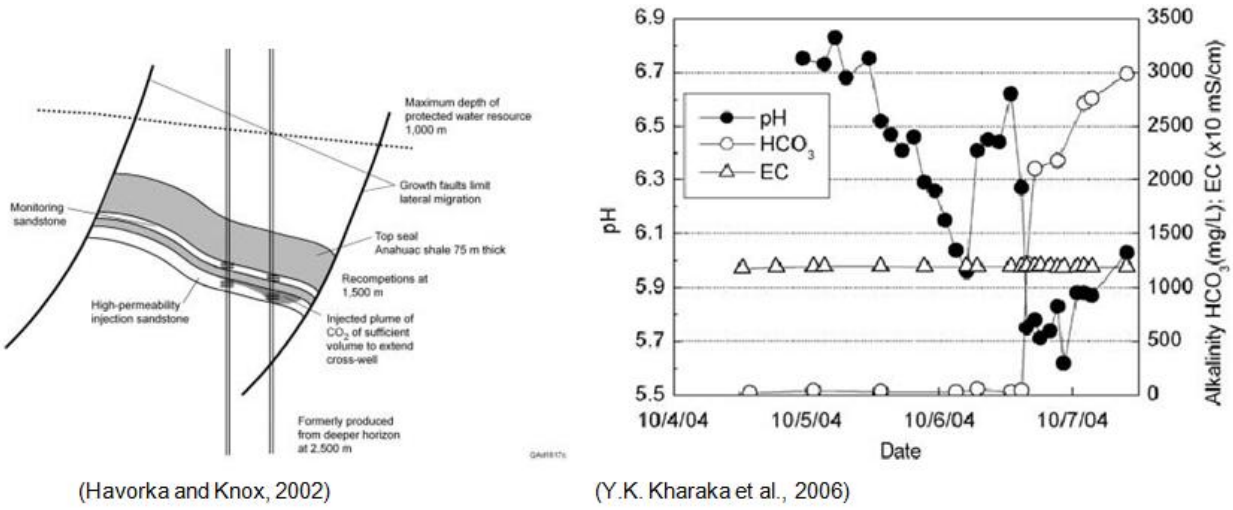

(Havorka and Knox, 2002) (Y.K. Kharaka et al., 2006)

Figure 13. The motivation for one particular problem students investigated focused on explaining why the Frio Brine Pilot experiment showed a pH decrease before the arrival of HCO_3^-.

The students used the Web-app to investigate such phenomena and developed a model that characterizes the displacement of the H^+ diffusion front that forms ahead of the advective front as a function of reservoir temperature and seepage velocity. These findings, based on data collected by students using our Web application, were presented at the 10th Annual Conference on Carbon Capture and Sequestration in Pittsburgh, Pennsylvania [2]. Additionally, the students each ran 50-100 simulations with varying reservoir temperatures and seepage velocities and generated 2D plots showing the difference in length between the H^+ ion diffusion front and the sweep front defined by the injectant water. An H^+ ion diffusion front is formed when CO_2-rich water is injected into brine formation water in sandstone. Students used the Web-app to configure a 1D horizontal simulation with reservoir temperatures varying from 20°C to 120°C, and specified a water mixture containing $CO_{2(aq)}$ be injected at seepage velocities of 100, 200, 300, 400, and 500 [cc/(cm2 yr)]/φ for 5 years. The CO_2-rich injectant water was modeled as a mixture of the formation water and a 0.5M solution of $CO_{2(aq)}$ with an $5.0x10^{-5}$M concentration of iron used as a non-reactive tracer to mark the location of the effluent. The compositions of the formation and injectant waters are given in Table 1; the composition of the lithology used to model the Frio Brine Pilot simulation is given in Table 2.

Table 1. Formation and injectant water compositions used to model the Frio Brine Pilot simulation.

Ion	Formation Water	Injectant Water
pH	5.59	5
$CO_{2(aq)}$	total 0.002M	Total 0.5M
HCO_3^-		
CO_3^{--}		
Ca^{++}	0.0025 M	0.0025 M
$Al(OH)_3$	1.7x10-6 M	1.7x10-6 M
K^+	5.0x10-5 M	5.0x10-5 M
$SiO_{2(aq)}$	0.001 M	0.001 M
Na^+	0.4 M	0.4 M
Cl^-	0.4 M	0.4 M
Fe^{++}	1.0x10-5 M	5.0x10-5 M
Mg^{++}	1.0X10-4 M	5.0x10-4 M

Table 2. Lithology composition used to model the Frio Brine Pilot simulation.

Mineral	Volume (%)	Grain Radii (cm)
Quartz	0.45	0.0200
k-feldspar	0.10	0.0300
Anorthite	0.05	0.0300
Albite	0.02	0.0300
Calcite	0.05	0.0010
Kaolinite	0.02	0.0001
Smectite	0.00	0.0001
Illite	0.00	0.0001
Halite	0.00	0.0100

With this configuration, students found that a distinct advective front develops ahead of a diffusive front when CO_2-rich water displaces the formation water. Differences in diffusivities of solutes are the most likely cause of the front separation. The diffusivity of the H^+ ion is an order of magnitude greater than the Fe^{++} ion. A screenshot from the Web-app showing the combined concentrations [H^+] and [Fe^{++}] are shown in Figure 15. Students found that this separation distance changes in time as a function of reservoir temperature and seepage velocity. It was hypothesized that this distance occurs when advective driven solute transport is less dominant than diffusive driven transport. Figure 16 shows the separation distance as a function of reservoir temperature and seepage velocity using data generated through the Web-app. One observes, by looking

at the separation surface, that a local minima is present at high temperatures and low injectant velocity. Further, a separation maxima propagates to a lower temperature region over time.

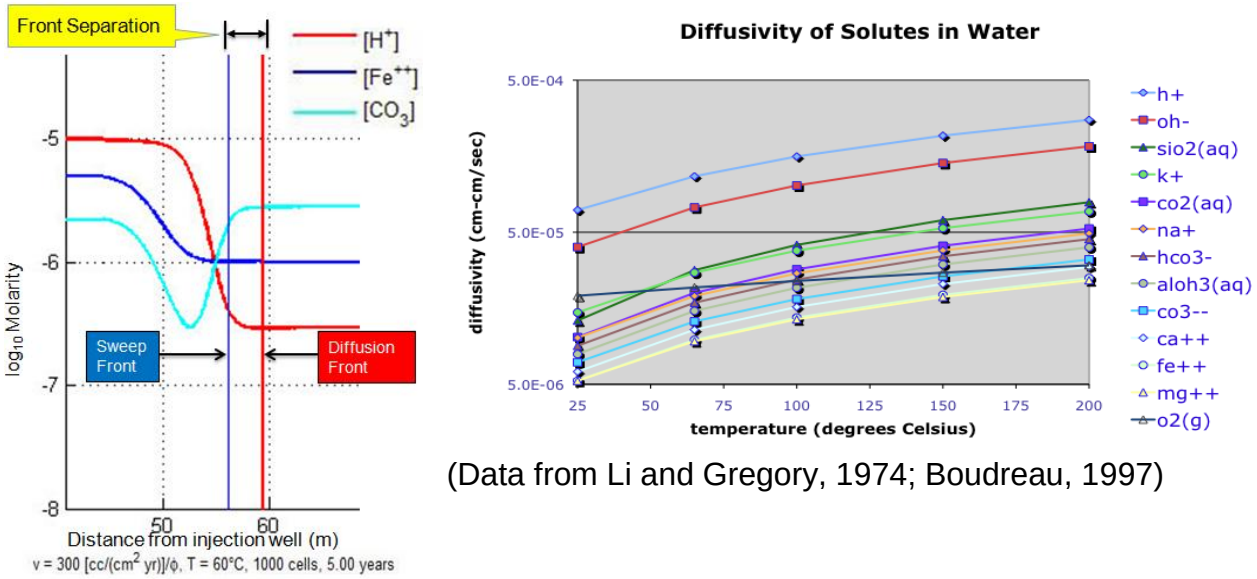

(Data from Li and Gregory, 1974; Boudreau, 1997)

Figure 14. A distinct advective front of H^+ develops in front of a diffusive front of injectant, indicated by a moving higher concentration of non-reactive Fe^{++} ion when CO_2-rich water displaces the formation water. Concentration profile shown for the simulation case with an injectant velocity of v_x=300 cm/yr/φ and 1000 computational control volumes. Separation distance is shown at simulated year 5.

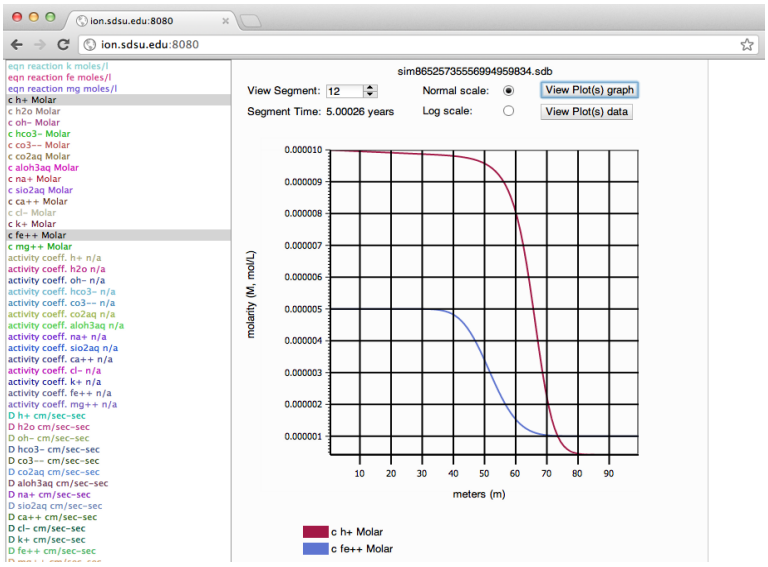

Figure 15. Screenshot from the Web-app showing the combined concentrations [H^+] and [Fe^{++}]. The Web-app allows any number of simulation properties to be selected from the scrolled list on the left and plotted. Normal and log scale plots are supported by togging a radio button.

A second problem students were asked to evaluate in the course was to investigate vertical CO_2 diffusion through three different lithologies. The motivation for this scenario was to determine if a low permeability shale layer would sufficiently retard CO_2 transport as to not lower the pH of the water in an upper permeable and porous sandstone lithology. We assume that a fresh water aquifer resides in the upper sandstone layer. The students configured this problem as a pure diffusion problem by specifying a seepage velocity v_x= 0 m/s and simulated with a reservoir temperature of 60°C.

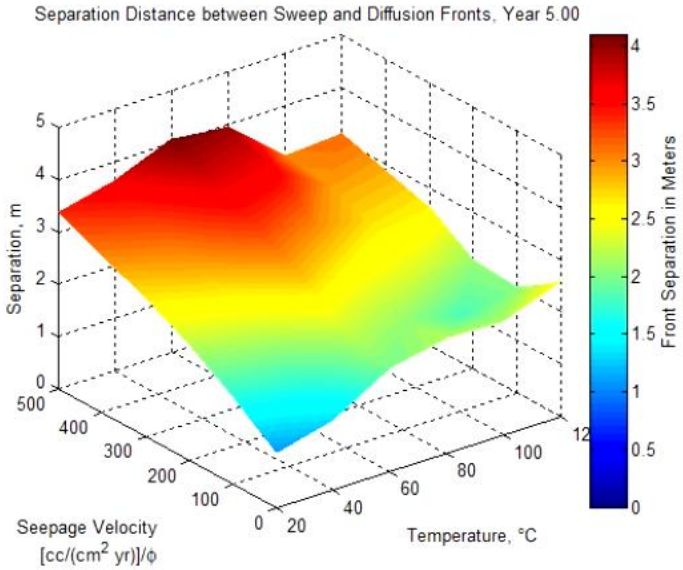

Figure 16. Separation distance as a function of reservoir temperature and seepage velocity.

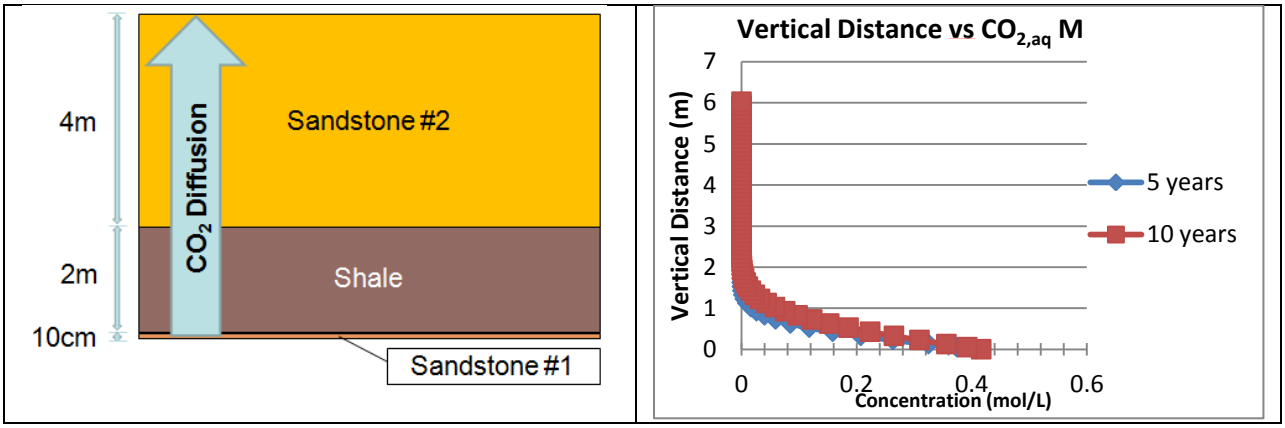

The simulation data accumulated from this exercise was compiled into a conference paper and presented at the AIAA 9th Annual International Energy Conversion Engineering Joint Conference held July 31 through August 3, 2011, in San Diego [3].

Another exercise was to simulate the vertical diffusion of aqueous CO_2 through three different lithologies consisting of a shale layer sandwiched between two sandstone layers. The students used the Web-based simulator to configure a domain consisting of three lithologies and two water mixtures. The students then used the simulator to compute the molarity of $CO_{2(aq)}$ and activity of H^+ with respect to vertical distance over a 5 and 10 year period. The students were asked to discuss how well the shale layer retarded CO_2 diffusion and to assume there was a freshwater aquifer above the upper sandstone lithology and determine if the pH of the water at the top of the sandstone was unacceptably low.

An additional interesting problem the students worked on involved Liesegang banding. In this exercise, the students used the Web-based simulator to configure a domain consisting of a single 5m sandstone lithology with three water mixtures: the resident water, a mixture rich in iron (Fe^{++}) ion flowing in one direction, and a mixture rich in oxygen gas flowing in an opposed direction. After 10 years, natural patterns form from the precipitation of iron(III) oxide (Fe_2O_3) in the sandstone. These patterns form as a result of naturally occurring geologic processes. Students configured a seepage velocity v_x=0.35 m/yr/φ, a reservoir temperature T_{res}= 60°C, a reservoir depth D_{res}=2000m, and 200 computational control volumes. The lithology was configured to consist of a volume fraction of 65% quartz with a grain radius of 0.02mm. To simulate the precipitation of hematite, students configured three different mixtures of water as given in Table 3. The formation water is the initial mixture composition in the reservoir, the *backflow* is a different mixture that moves from right to left in the negative x-axis direction, and the *injectant* is another different mixture that moves from left to right in the positive x-axis direction. Patterns of iron oxide can occur in permeable rocks that undergo a chemical weathering process, such as the intersection of oxygenated water with a different source of water containing a high concentration of iron. A cartoon depicting this process is shown in Figure 17.

Table 3. Solute concentrations in the formation, backflow (right to left transport), and "injectant" (left to right transport) water mixtures.

Solute	Formation, M	Backflow, M	Injectant, M
$SiO_{2(aq)}$	0.0001	0.0001	0.0001
H^+	2.1e-07	2.1e-07	1.1e-05
H_2O	1	1	1
$O_{2(g)}$	1.0e-08	1.0e-08	5.0e-14
Fe^{++}	4.0e-19	4.0e-19	6.6e-14

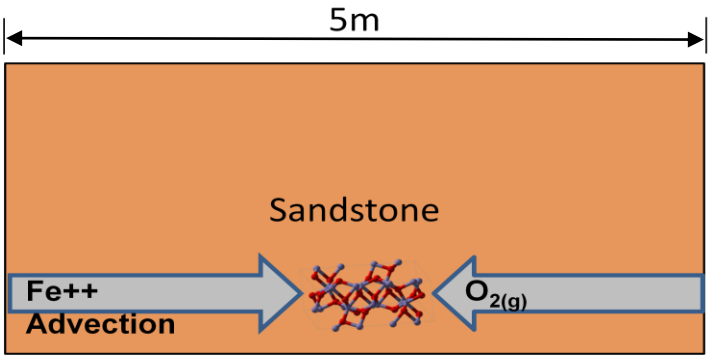

Figure 17. Patterns of iron oxide can occur in permeable rocks that undergo a chemical weathering process, such as the intersection of oxygenated water with other water containing a high concentration of iron.

By specifying a large number (~200) of computational cells, hematite pattern formation becomes apparent after 10 years. Hematite precipitation occurs where the saturation value > 1, as shown in Figure 18.

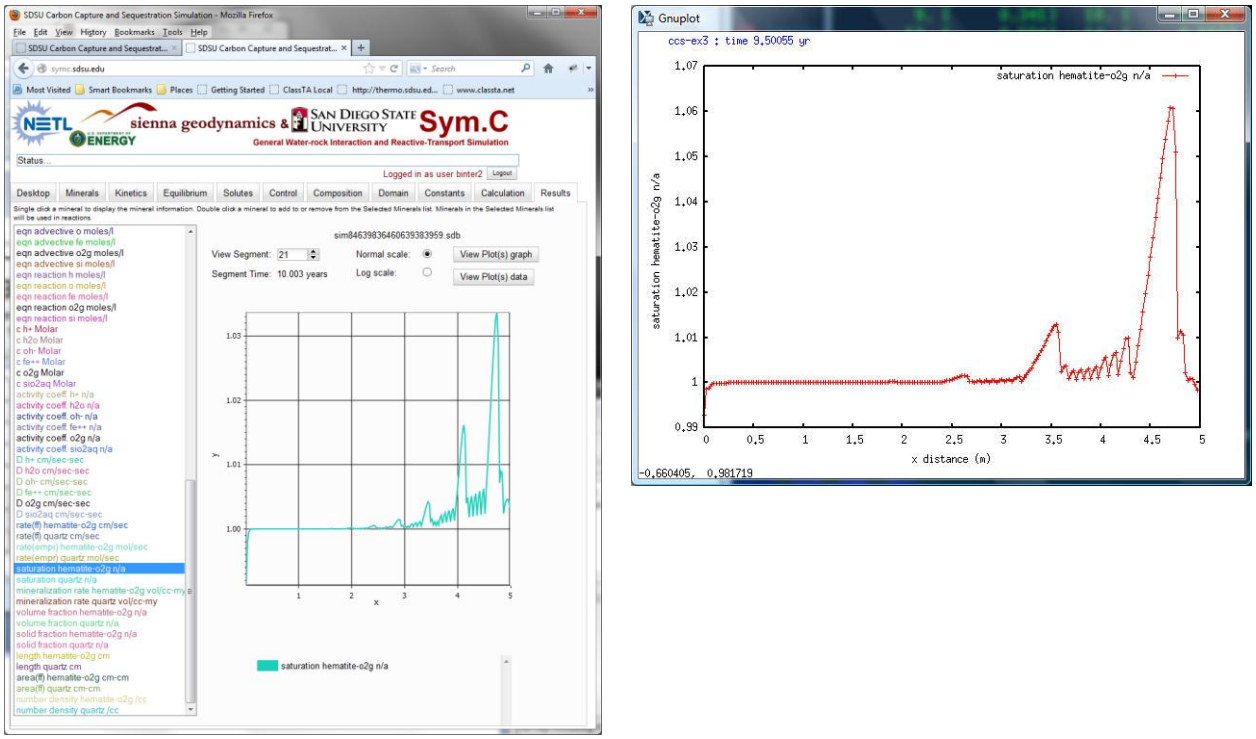

Figure 18. Plot of hematite precipitation as shown directly in the Web-app (left) and using Gnuplot from data downloaded from the RIA (right). Hematite precipitation occurs in the sandstone where the saturation value > 1.

Although not a CCS problem per se, it was interesting to show how the Web-based simulator we have developed can be used to solve and visualize remarkable geochemical problems.

Results and Discussions

Geomechanical Modeling

One of the goals of this project was to adapt the Web interface to include other types of modeling including thermal and geophysical. The water-rock interaction core simulator used by the Web application solves a chemical element conservation equation, given by

$$\frac{\partial e_\beta}{\partial t} = \sum_{\alpha=1}^{Na} \nu_{\beta\alpha} \left[\phi D_\alpha \nabla^2 c_\alpha - \phi \vec{\nabla} \bullet \left(c_\alpha \vec{u} \right) \right] - \sum_{\gamma=1}^{M} \nu_{\beta\gamma} \rho_\gamma A_\gamma G_\gamma \quad (1)$$

where the evolution of chemical elemental mass e_β depends on mass-transfer from diffusive and advective forces as well as the precipitation and dissolution of minerals governed by kinetic reaction rates. In equation (1), $\nu_{\beta\alpha}$ is the reaction stoichiometric term equal to the number of atoms of element β in solute species α, ϕ is porosity, D_α is the diffusion coefficient of solute species α, c_α is the concentration (molarity) of solute species α, $\vec{u}$ is the velocity of the CO_2-rich water injectant, ρ_γ is the mineral solid molar density of mineral γ, A_γ is the surface area of mineral γ, and G_γ is the reaction rate of mineral γ. Currently, the core simulator uses a second order central differencing scheme to discretize the diffusive term of the conservation equation and a first order upwind scheme to discretize the advective term. Under the direction of the PIs, doctoral student Eduardo J. Sanchez Peiro has replaced the second order central differencing scheme in Sym.8 with a fourth order mimetic scheme. A numerical method is called *mimetic* if it (1) produces discretizations on a staggered grid for the operators *G*, *D*, and *B*, where these operators are, respectively, the gradient, divergence, and boundary normal derivative operators, and (2) satisfies the generalized Green's identity

$$(\mathbf{D}\boldsymbol{v}, \boldsymbol{f})_{\boldsymbol{Q}} + (\boldsymbol{v}, \mathbf{G}\boldsymbol{f})_{\boldsymbol{P}} = (\mathbf{B}\boldsymbol{v}, \boldsymbol{f}) \quad (2)$$

for a convenient inner product $(\,.\,,\,.\,)$, where **P** and **Q** are weights. Using a mimetic approach, a higher-order approximation to the derivatives in our chemical element conservation equation can be constructed that satisfy the global conservation law. Specifically, fourth order approximations to both the divergence and the gradient operators in the grid interior and on the boundary can be constructed. This approach generalizes to higher-order approximations. In fact, it is possible to extend this scheme to obtain sixth-order approximations on a one-dimensional uniform grid.

Eduardo J. Sanchez Peiro has modified the core simulation code to use LAPACK version 3.3.1 (http://www.netlib.org/lapack/) and SuperLU DIST (http://crd.lbl.gov/~xiaoye/SuperLU/) for solving the large sparse systems of equations constructed during each iteration. Eduardo presented this work while participating in the Broader Engagement Program of the International Conference for High Performance Computing, Networking, Storage and Analysis (SC11) that took place November 12-18, 2011 in Seattle. Eduardo presented a poster comparing the speedup

and efficiency of running our water-rock interaction code on the TeraGrid server *trestles.sdsc.edu*. The Computational Science Research Center hosted a table at SC11 where our WebSimC Web application was available for demonstration by conference attendees. Trestles is a dedicated TeraGrid cluster at the San Diego Supercomputer Center and consists of 10,368 total cores with a theoretical peak performance of 100 TFlop/s. Eduardo compared the use of the standard LU factorization routine from Numerical Recipes [4], the LU solver provided in LAPACK, and SuperLU. We used a Black River - Maquoketa Interaction test case developed by Dr. Anthony Park to generate speedup and efficiency plots. The Black River - Maquoketa case is a CO_2-water-rock interaction study of the lower Paleozoic strata of the Illinois Basin in Kentucky that was conducted by Dr. Anthony Park, Dr. Thomas M. Parris, and Dr. John R. Bowersox. This 1000 simulation year case looks at geochemical changes that may occur in the Maquoketa formation water that resides above the Black River, should the Black River and lower Knox Group be used as a CCS target where CO_2 charged water is introduced. The Knox Group in central Kentucky consists of Cambrian and Ordovician carbonate rocks and is covered by Ordovician limestone and shale of the Black River and Maquoketa Formations. A 1000 year simulation was run for several days on symc.sdsu.edu where LU decomposition was performed serially. Eduardo executed a 10,000-year simulation of the Black River - Maquoketa case on Trestles with SuperLU enabled and evaluated the speedup of the parallel implementation. During the week of August 8 - 12, 2011, Eduardo and Co-PI Paolini presented posters at the eighth Annual Cyberinfrastructure Summer Institute for Geoscientists (CSIG'11) and the Gordon Summer Institute, which took place at the San Diego Supercomputer Center, University of California, in San Diego. At this workshop, we presented our work on sweep and diffusion front displacement as a function of reservoir temperature and seepage velocity, as well as our current development of a water-rock interaction code that uses a mimetic finite difference method to simulate geochemical changes that result from the injection of CO_2-rich water in brine reservoirs.

Eduardo also developed the *MTK* (Mimetic Methods Toolkit), an object-oriented applications programming interface, which allows an intuitive implementation of mimetic discretization methods. This tool kit is linked with Sym.8 to provide methods for the mimetic solution of advection-diffusion-reaction equations. Eduardo also improved the linear solver in Sim.8 by integrating the LAPACK library into the codebase. Since LAPACK is a FORTRAN library, a C wrapper library was required so it can be used in Sim.8, since Sim.8 is written in C. Eduardo used the ATLAS (Automatically Tuned Linear Algebra Software) C-wrapper which provides an optimized configuration of LAPACK for use on our 64-core Linux cluster, *blackbox.sdsu.edu*, which is used to run Sim.8. Blackbox has eight Intel Xeon E5420 2.50 GHz CPUs, with 6144 kB of cache memory. Eduardo compiled the results of ATLAS performance tests, shown in Table 4, executed on blackbox.

Table 4. Results of ATLAS performance tests executed on blackbox.sdsu.edu.

Reference clock rate=2394Mhz, new rate=2493Mhz Reference : Percentage of clock rate achieved by reference install Present : Percentage of clock rate achieved by present ATLAS install								
Benchmark	Single precision				Double precision			
	Real		Complex		Real		Complex	
	Reference	Present	Reference	Present	Reference	Present	Reference	Present
kSelMM	**565.9**	**589.2**	**532.9**	**559.4**	365.5	364.1	**334.8**	**352.9**
kGenMM	177.6	163.6	177.6	170.8	**166.1**	**166.7**	162.6	143.4
kMM_NT	**134.0**	**153.1**	**138.9**	**157.8**	**119.1**	**147.4**	**137.6**	**143.4**
kMM_TN	**159.3**	**166.6**	165.6	163.1	**148.2**	**159.6**	159.0	157.4
BIG_MM	**558.5**	**571.8**	**557.8**	**580.7**	353.8	265.0	346.7	342.2
kMV_N	111.0	78.3	211.1	140.0	55.2	45.9	92.8	64.8
kMV_T	85.0	77.0	**93.1**	**99.8**	**45.5**	**47.2**	76.7	66.7
kGER	**159.0**	**190.4**	**119.0**	**142.6**	**27.8**	**39.0**	**46.5**	**54.8**

Eduardo added an ability in Sym.8 to use any one of four linear system solvers during a simulation:

1. the default solver, based on the LU factorization algorithm presented in the Numerical Recipes textbook [4],
2. the ATLAS optimized LU factorization algorithm provided by LAPACK,
3. the sequential implementation of the SuperLU solver developed by X. Sherry Li at Lawrence Berkeley National Laboratory, and
4. the distributed implementation of SuperLU for running Sym.8 on multicore clusters.

The matrices generated to solve for solute concentrations are sparse matrices, which allow us to exploit the capabilities provided by the sequential and distributed SuperLU library provided by the Lawrence Berkeley National Laboratory. SuperLU is a general-purpose library for the direct solution of large, sparse, nonsymmetric systems of linear equations on high performance machines [5]. The library routines perform LU decomposition with partial pivoting and triangular system solves through forward and back substitution. The LU factorization routines can handle non-square matrices but the triangular solves are performed only for square matrices.

Table 5. Wall clock time comparison of running the 1D simulation using the indicated linear solver. Units are in hours:minutes:seconds.centiseconds.

Cells:	100	1,000	10,000
Reference	33:18.88	2:48:31.98	35:49:11.67
ATLAS	30:46.24	2:14:17.59	16:42:03.08
SuperLU	44:34.27	3:11:51.27	34:39:21.37

Attained speedup for sequential SuperLU over the reference algorithm is not significant, given the nature of the involved matrices, which limits the size to the number of aqueous solutes being solved (14 solutes in this particular simulation). To exploit the

capabilities of Super LU, Eduardo implemented a new scheme that takes advantage of the distributed implementation of SuperLU for running Sym.8 on the multicore SDSC TeraGrid/XSEDE system *trestles.sdsu.edu* named *BLOGS* for Block-defined Global Sparse Scheme, which is a parallel large-sparse system solver module. Eduardo implemented the following global scheme to solve for the mass-transfer chemical system in parallel:

$$\begin{bmatrix} J_{1,1} & Jt_{2,1} & 0 & 0 & 0 \\ Jt_{1,2} & J_{2,2} & Jt_{3,2} & 0 & 0 \\ 0 & Jt_{i-1,j} & J_{i,j} & Jt_{i+1,j} & 0 \\ 0 & 0 & \ddots & \ddots & \ddots \\ 0 & 0 & 0 & Jt_{N-1,N} & J_{N,N} \end{bmatrix} \begin{bmatrix} \underline{c}_1 \\ \underline{c}_2 \\ \underline{c}_i \\ \vdots \\ \underline{c}_N \end{bmatrix} = \begin{bmatrix} \underline{f(c)}_1 \\ \underline{f(c)}_2 \\ \underline{f(c)}_i \\ \vdots \\ \underline{f(c)}_N \end{bmatrix}$$

where

- $J_{i,j}$ is a sparse block sub matrix of dimension (a x a) from reaction terms and diffusion and advection terms for cell (control volume) i,
- $Jt_{i,j}$ is a banded diagonal block constructed from diffusion and advection terms for cells $i+1$ and $i-1$,
- c_i is a vector of length a for the unknown concentration of a solutes in cell i,
- $f(c)_i$ is a vector of solute equilibrium reaction source terms evaluated for cell i

The general idea is to produce a large block-banded sparse matrix of rank (a x N)^2, where a is the number of solutes and N is the number of control volumes used to discretize the domain (geologic reservoir). This new scheme is termed the *BLOGS scheme* for *Block-defined Global Sparse Scheme*,

$$\begin{bmatrix} \mathbf{W}_{1,1} & \mathbf{W}_{1,2} & & & \cdots & & \mathbf{W}_{1,N} \\ \mathbf{B}^{w}_{2,1} & \mathbf{B}^{0}_{2,2} & \mathbf{B}^{e}_{2,3} & & & & \\ & \mathbf{B}^{w}_{3,2} & \mathbf{B}^{0}_{3,3} & \mathbf{B}^{e}_{3,4} & & & \\ & & \ddots & \ddots & \ddots & & \\ & & & \mathbf{B}^{w}_{i,j-1} & \mathbf{B}^{0}_{i,j} & \mathbf{B}^{e}_{i,j+1} & \\ & & & & \ddots & \ddots & \ddots \\ \mathbf{E}_{N,1} & & \cdots & & & \mathbf{E}_{N,N-1} & \mathbf{E}_{N,N} \end{bmatrix} \begin{bmatrix} \mathbf{c}_w \\ \mathbf{c}_2 \\ \mathbf{c}_3 \\ \vdots \\ \mathbf{c}_e \end{bmatrix} = \begin{bmatrix} \mathbf{r}(\mathbf{c}_w) \\ \mathbf{r}(\mathbf{c}_2) \\ \mathbf{r}(\mathbf{c}_3) \\ \vdots \\ \mathbf{r}(\mathbf{c}_e) \end{bmatrix} \quad (3)$$

where the block sub-matrices are defined as,

$\mathbf{B}^{0}_{i,j}$ is a sparse, diagonal block of dimension $(N_a \times N_a)$ from discretization terms at the *i*-th node. $\mathbf{B}^{w}_{i,j-1}$ and $\mathbf{B}^{e}_{i,j+1}$ are both sparse and diagonal blocks of dimension $(N_a \times N_a)$ from discretization terms at both the west-neighboring (*w*) node and the east-neighboring (*e*) node. $\mathbf{W}_{1,1}$ to $\mathbf{W}_{1,N}$ are sparse and diagonal blocks of dimension $(N_a \times N_a)$ from discretization terms at both the west boundary. These comprise the first N_a rows of the matrix. $\mathbf{E}_{N,N}$ to $\mathbf{E}_{N,1}$ are sparse and diagonal blocks of dimension $(N_a \times N_a)$ from discretization terms at both the east boundary. These comprise the last N_a rows of the matrix. $\mathbf{c}_i$ is the vector of length N_a of all the concentration variables at node *i*. $\mathbf{r}(\mathbf{c}_i)$ is the vector of length N_a of all the contributions from considered reactions, also at node *i*.

Such very-large, sparse, banded matrices can be solved, efficiently and in parallel, using the distributed implementation of Super LU, the distributed memory version of SuperLU [6]. Eduardo performed a speedup and efficiency analysis to compare the performance of running Sim.8 sequentially using the Numerical Recipes reference solution, the ATLAS optimized LAPACK solution, and the sequential SuperLU solution compared with the distributed SuperLU solution. Test cases were run on *trestles.sdsc.edu*, an XSEDE resource located at the San Diego Supercomputing Center, which will be accessed from SDSU via CSRCnet, an NSF funded high-speed network, which allows high performance connectivity between San Diego State University and the San Diego Supercomputing Center.

Eduardo was accepted into the highly competitive Research Experience in Carbon Sequestration (RECS) 2012 program held June 3-13, 2012 in Birmingham, Alabama. RECS is a DOE/NETL sponsored intensive 10-day summer program that fosters and advances education, scientific research, professional training, and career networks for graduate students and young professionals in the carbon capture, utilization and storage (CCUS) field (http://www.recsco2.org/). Through the direct training and research experience Eduardo gained from participating in this DOE project, Eduardo was chosen to attend the 2012 RECS program, an honor since RECS exercises a very competitive candidate selection process that is limited to 30 participants.

Master of Science in Geological Science candidate Christopher Binter worked closely with Co-PI Paolini and developed a heat transfer module in Sym.8. Christopher implemented a module that solves a heat convection-diffusion equation using Spalding and Patankar's Semi-Implicit Method for Pressure Linked Equations (SIMPLE) algorithm, commonly used in computational fluid dynamics codes to simulate heat transfer in fluid flow scenarios. Coupled with the elemental mass-transport equation (1) being solved in Sym.8, Binter implemented a one dimensional heat transport model, given canonically as

$$\frac{\partial}{\partial t}(\rho T)+\frac{\partial}{\partial x}(\rho u T)=\frac{\partial}{\partial x}\left(\Gamma\frac{\partial T}{\partial x}\right)+S_T \tag{4}$$

where the source term S_T is computed using the *Helgeson-Kirkham-Flowers* (HKF) model for computing thermodynamic properties of aqueous electrolytes. The numerical implementation uses a finite volume formulation that Binter and Paolini have implemented in Sym.8 as a heat transfer module. The module uses a finite volume scheme, where the advective (*F*) and diffusive (*D*) heat flux per unit area at each cell face is computed and then a central differencing scheme is used to solve for temperature in each cell interior, where cells are modeled as adjacent parallelepipeds, shown in Figure 19.

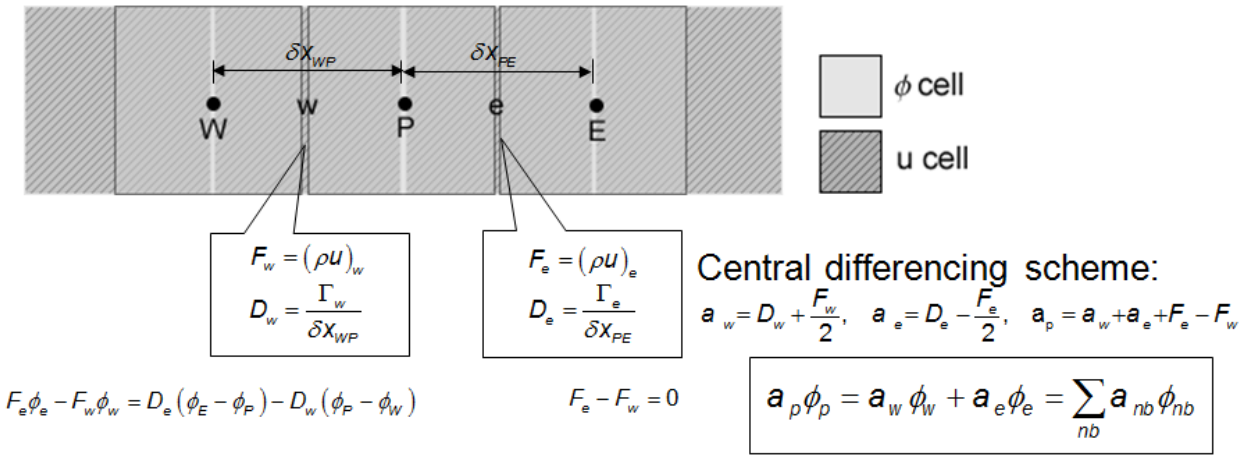

Figure 19. Binter and Paolini implemented a numerical heat transfer module in Sym.8 that uses a finite volume scheme where the advective (*F*) and diffusive (*D*) heat flux per unit area at each cell face is computed and then a central differencing scheme is used to solve for temperature in the interior of each cell.

The source term S_T in (4) is calculated using the Helgeson-Kirkham-Flowers (HKF) model for computing thermodynamic properties of aqueous electrolytes,

$$S_T=\frac{dT}{dt}=-\left(\frac{1}{C_p(T)}\right)\sum_{j=1}^{NS}\left(\frac{dc}{dt}\right)_j\bar{h}_j(T);\quad\left[\frac{gK}{m^3 s}\right] \tag{5}$$

where

$$C_p(T)=\sum_{j=1}^{NS}n_j\bar{c}_{p,j}(T), \tag{6}$$

$(dc/dt)_j$ is the rate of change of the j^{th} solute species concentration at time t, n_j is the number of moles of the j^{th} solute species in the reservoir water, $\bar{c}_{p,j}$ is the *volumetric* molar heat capacity of the j^{th} solute species, C_p is the total volumetric heat capacity of the reservoir water, and $\bar{h}$ is the molar enthalpy of the j^{th} solute species. The source

term represents the energy generation as heat, resulting from a change in solute concentration. Thermodynamic properties, such as the molar heat capacity, molar volume, and molar enthalpy of charged aqueous solute species, are computed using the Helgeson-Kirkham-Flowers (HKF) Model. For example, the HKF model for molar heat capacity specifies

$$\bar{c}_p = c_1 + \frac{c_2}{(T-\Theta)^2} - \frac{2T}{(T-\Theta)^3}\left[a_3(P-P_r) + a_4 \ln\left(\frac{\Psi+P}{\Psi+P_r}\right)\right] + \omega TX + 2TY\left(\frac{\partial \omega}{\partial T}\right)_P - T(Z-1)\left(\frac{\partial^2 \omega}{\partial T^2}\right)_P \quad (7)$$

where

Ψ is solvent pressure (2600 bar)
Θ is water singularity temperature (228K)
P_r is reference pressure (1 bar)
P is simulation pressure (bar)
T is simulation temperature (K)
ω is Born coefficient (J/mol)
ε is permittivity of H2O (-)
Z, Y, X are the Born functions (-), (1/K), ($1/K^2$)

The relative permittivity (dielectric constant) of H_2O, the Born coefficient, and the Born functions are also calculated using the HKF model for a given temperature, pressure, and density. The plot of an example temperature profile using the SIMPLE-HKF scheme is shown in Figure 20. This plot is based on a simulation with v_x=30 cm/yr/φ, a 3M $CO_{2(aq)}$ injectant water composition, and a reservoir temperature T_{res}=59°C.

The temperature module iteratively calculates thermophysical properties of charged aqueous solutes and uses these properties to compute a spatial and temporal temperature profile. An advection-diffusion model governing heat transport is solved using a finite volume method with solute specific partial molal enthalpy and partial molal heat capacity values obtained using the Helgeson-Kirkham-Flowers (HKF) model. The temperature module has been used to study temperature effects resulting from injection of CO_2-rich water into the Oligocene Frio formation along the Texas Gulf Coast, with simulation parameters similar to the Frio Test Pilot Experiment. Simulation results were compared to bottom hole temperature data obtained from an observation well 30 meters away from the injection well during the injection phase. Results show an increase in temperature caused by the arrival of the CO_2-rich injectant that is in agreement with the well data. Results further show small variations in injection rate and pressure have little effect on the temperature increase, while changing total carbon concentration in the injectant water has a direct impact on temperature. The simulated temperature profile correlates with other simulation results that show an increase in temperature resulting

from CO_2 injection. Temperature signatures predicted by numerical simulation could be used to monitor the migration of CO_2-rich plumes. This module can also be used to conduct *what-if* scenarios to determine the maximum amount of CO_2 that can be sequestered in a formation without exceeding a critical reservoir temperature that could damage instruments and seals.

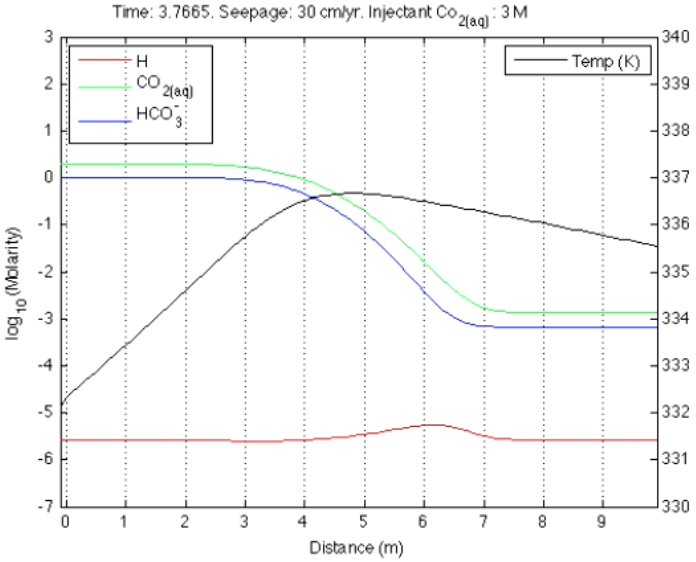

Figure 20. Example temperature profile using the SIMPLE-HKF scheme with v_x=30 cm/yr/φ, a 3M $CO_{2(aq)}$ injectant water composition, and a reservoir temperature T_{res}=59°C.

Simulations were run to test the validity of the 1D temperature module. The injection rate, porosity, lithology, water chemistry, temperature, pressure and simulation time were modeled after the Frio Test Pilot Experiment. In the Frio Test Pilot Experiment, an increase in bicarbonate from 100mg/L to 3000 mg/l was interpreted as representing the arrival of the injectant [1]. This increase was observed approximately 2 days after injection began, in the observation well located 30 meters away. Thus, an injection rate of 15 meters/day was used. The simulation temperature was set to 58.55˚C and the simulation pressure was set to 148.319 bars, which was the temperature and pressure in the observation well when injection began at 11:34 am on October 4th, 2004 (Table 6). The simulations were run for 30 days, which is slightly longer than the time it took the Frio Test Pilot observation well to reach a semi-equilibrium temperature. Lithology and water chemistry properties were set similar to values used by Xu et al. [7] to model the Frio Formation (Table 8, Table 9). Multiple Frio simulations were run with small variations in injection rate, pressure, total inorganic carbon content, and initial temperature to study effects on the overall temperature profile.

Table 6. Simulation physical parameters.

Parameter	Model Value
Porosity	0.34
Permeability	11.3 mD
Temperature	58.55˚C
Pressure	148.319 bar
Advective Velocity	15 meters/day

Two different simulations were run at the injection rate observed at the Frio Formation (~15 meters/day) and temperature data was recorded 30 meters away from the injection well, where the observation well in the Frio Test Pilot Experiment resided. To study the temperature effects from CO_2 injection only, a lithology consisting entirely of quartz was selected. A lithology consisting entirely of quartz was first selected because of the relatively long timescale for quartz precipitation or dissolution, thus the only change in solute concentrations would result from CO_2 injection. The lithology was composed of 66% volume fraction of quartz to match the Frio Formation, and the relatively long timescale for quartz precipitation or dissolution ensured that the only change in solutes would result from CO_2 injection. The formation and injectant water pH and total inorganic carbon values were selected to match the pH and total inorganic carbon values of the Frio Test Pilot Experiment. $SiO_{2(aq)}$ concentrations were obtained by running the simulation with no injection until the system reached equilibrium and $SiO_{2(aq)}$ concentrations did not change. Table 7 shows the formation and injectant water compositions used in the quartz-only simulations. All other solutes besides those listed were removed so that the amount of heat change can be attributed to only changes in total inorganic carbon resulting from injection.

Table 7. Quartz only simulation water compositions.

Formation Water Composition		Injectant Water Composition	
Solute	Concentration (Molarity)	Solute	Concentration (Molarity)
H_3O^+	3.16E-7	H_3O^+	1.0E-6
$SiO_{2(aq)}$	2.95658E-4	$SiO_{2(aq)}$	2.95658E-4
$CO_{2(aq)}$	0.000396886	$CO_{2(aq)}$	0.0375561
HCO_3^-	0.00163839	HCO_3^-	0.0491662
CO_3^{2-}	1.85531e-06	CO_3^{2-}	1.76526e-05

Frio Formation simulations were run to evaluate if WebSimC, with our temperature model, could reproduce the same temperature changes as measured in the Frio Brine Test Pilot experiment (Table 8, Table 9). As in the quartz only simulations, an initial

injection rate of 15 meters/day was used and the simulations were run for 30 days. Since the current model does not take into account changes in pressure, as TOUGHREACT does, and pressure's effect on advection, simulations were also run at 12, 7.5, 3.75, and 1.7 meters/day to study how changes in the advection rate affected the temperature profile. The Frio simulation lithologies were composed of nine minerals with a total volume fraction of 66%. Table 8 shows the minerals and volume fractions used in each Frio simulation. These minerals and volume fractions are similar to the volume fractions used by Xu et al. [7] in their modeling of the Frio Test Pilot Experiment. Hematite was not included because of WebSimC's inability to calculate accurately hematite dissociation and precipitation in reasonable computational time.

Table 8: Frio Test Pilot simulations minerals and volume fractions.

Mineral	Volume Fraction
Albite	10.50346
Anorthite	2.66464
Calcite	1.32484
Chlorite	3.05866
Illite	0.68134
K-feldspar	5.44984
Kaolinite	1.38160
quartz	38.25250
smectite	2.68312

The formation and injectant water temperatures were set to 58.55˚C, which was the down-hole temperature at the observation well when injection began at 11:34am on 10/4/2004 [1]. The pressure was set to 148.319 bars to match the initial measured Frio field. The Frio Formation and injectant water compositions were simulated using data from Kharaka et al. [1] and Xu et al. [7]. The concentration of solutes were obtained from fluid samples collected prior to CO_2 injection and used in RTM modeling by Xu. The injectant water used in the Frio Test Pilot Experiment was a mix of the formation water, with an increase in CO_2, thus solute concentrations of species other than H_3O^+, H_2CO_2, HCO_3^- and CO_3^{2-} were kept the same in the injectant and formation water. The pH and total inorganic carbon for the formation and injectant waters were simulated using data from Kharaka. HCO_3^- concentrations of 100 mg/L and a pH value of 6.5 was observed pre-injection and HCO_3^- concentrations increased to 3000 mg/L and the pH dropped to 6.0 with the arrival of the CO_2 rich injection front [1]. Given these HCO_3^- and pH values, total inorganic carbon was calculated for each water composition. Kharaka proposed that the decrease in pH could be caused by the mixing of the formation water with supercritical CO_2-rich injectant water. In this case, the dissociation of CO_2 would

produce hydronium ions that would decrease the pH. WebSimC is unable to model supercritical CO_2 at the present time, so we set the pH in the injectant water to 6.0.

Table 9: Frio Test Pilot Simulations Water Compositions

	Formation Water	Injectant Water
Solute	Concentration (Molarity)	Concentration (Molarity)
H_3O^+	3.16E-7	1.0E-6
Ca^{2+}	4.25132E-02	4.25132E-02
$Al(OH)_3$	3.66288E-08	3.66288E-08
k^+	9.03602E-03	9.03602E-03
$SiO_{2(aq)}$	4.16399e-05	4.16399e-05
$CO_{2\ (aq)}$	0.000396886	0.0375561
HCO_3^-	0.00163839	0.0491662
CO_3^{2-}	1.85531e-06	1.76526e-05
Na^+	9.89444E-02	9.89444E-02
Mg^{2+}	3.36584E-02	3.36584E-02
Fe^{2+}	1.05972E-03	1.05972E-03
Cl^-	6.50035E-02	6.50035E-02

After injection began on October 4th, the pressure increased to a maximum of 150.448 bars on 10/12/04. Because WebSimC did not, at the time, calculate changes in pressure resulting from injection, another Frio Test Pilot simulation was run with the pressure set to 150.448 bars instead of the initial pressure of 148.319 bars. The purpose here was to evaluate how the temperature profile changed with changes in pressure. Since the pressure increase between the initial and maximum pressure was only 2.129 bars resulting from the 10 days of injection, a third simulation was run at a pressure of 171.738 bars.

Variations in the amount of total inorganic carbon was also examined. Two additional simulations were run: one with half the total inorganic carbon and a second with double the total inorganic carbon of the Frio Test Pilot Experiment. The purpose here was to determine if changing the amount of sequestered CO_2 has an effect on the temperature, and if so, to what extent. Examination of the temperature values shows that when injection began at 11:34 am on October 4th, the temperature was 58.55˚C. The temperature then decreased to roughly 58.4˚C and stayed constant for approximately 2 days. An additional simulation was run with an initial temperature of 58.4˚C to examine what the temperature profile would look like with the lower temperature and what affect the decrease in temperature had on the overall temperature profile.

The temperature and HCO_3^- values, at the observation well from the quartz-only simulation calculated using a 1D transient and steady state heat transfer model, were plotted against time (Figure 21). No parameters were changed between the 1D transient and steady-state heat transfer simulations except the selection of the temperature solver. In both simulations, the bicarbonate concentration begins to increase at the observation well after approximately 2 days of injection, which approximately matches the Frio Test Pilot Experiment where they noted bicarbonate concentrations increasing after approximately 2.1 days.

The temperature calculated using the transient model is observed to increase from the initial temperature of 58.55˚C to a maximum of approximately 61.5˚C after 2.2 days. It was observed that, four days after injection started, the temperature returned to the initial temperature of 58.55˚C and there was little to no observed change in temperature or HCO_3^-- from five days to the end of the simulation of 30 days. The temperature profile calculated using the steady state model differs from the transient in that a temperature increase to approximately 60.25˚C is observed after 0.2 days and the temperature stays constant until 2 days after injection started. After 2 days of injection, the temperature decreases and returns to the initial simulation temperature of 58.55˚C at approximately 4 days. As in the transient model, there is little to no observed change in temperature or HCO_3^- from 5 days to the end of the simulation at 30 days.

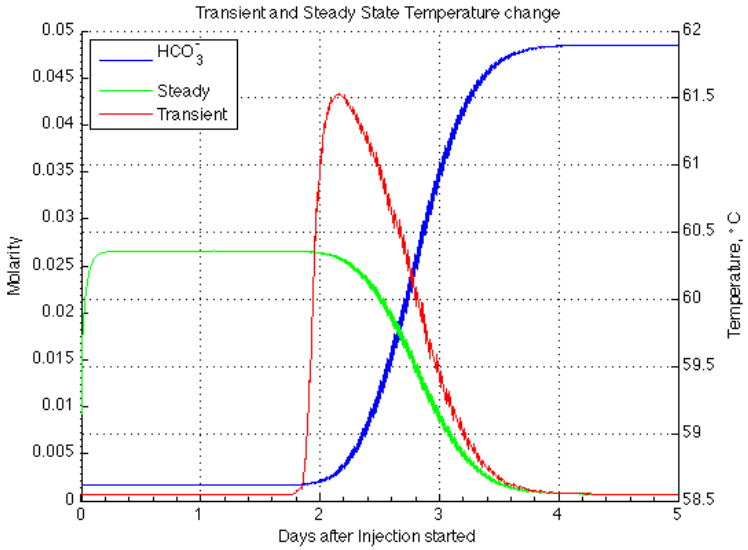

Figure 21. Transient and steady state model temperature comparison.

To evaluate the accuracy and validity of the developed model, temperature data from the Frio Test Pilot observation well was compared to the temperature profile calculated by WebSimC. A comparison of bottom hole temperatures from Frio Test Pilot observation well and the simulation calculated temperature for various grid cell sizes

were compared (Figure 22). The temperature points plotted are the observed and modeled temperature at the observation well plotted against time. The Frio simulations were run with three different grid cell sizes: 1.0, 0.5 and 0.25 meters. The importance of this is to show that the grid cell size has little effect on the overall temperature profile. In all three simulations, the temperature begins to rise approximately 2.1 days after injection. The temperature increases until thermal equilibrium is reached at approximately 59.05˚C on 10/7/2004. This is in contrast to the Frio field data that shows an initial decrease in temperature to approximately 58.4˚C, before a large decrease in temperature on 10/6/04 to 57.6˚C. After the large drop in temperature, the Frio field data show an increase in temperature until it reaches a semi equilibrium temperature of 58.75˚C on 10/25/04.

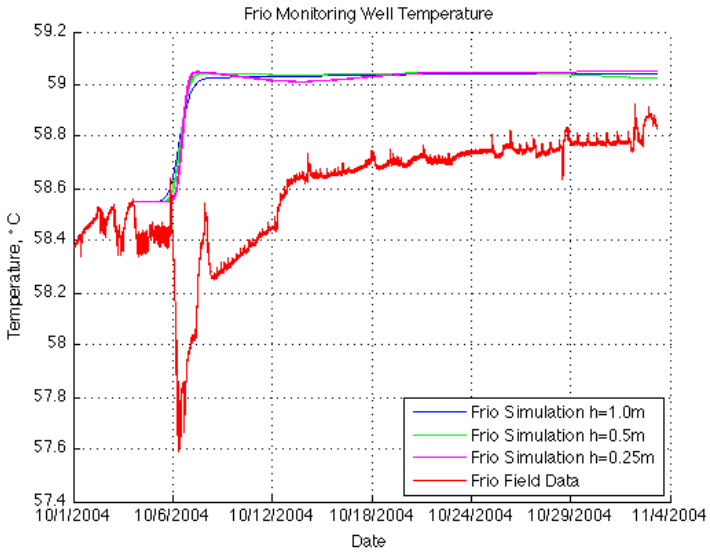

Figure 22. Frio field data from observation well and Frio simulation temperature for various grid cell sizes.

Images of solute concentrations and temperature for grid cells between 0 and 60 meters, at approximately 1, 2, 3 and 4 days, were generated (Figure 23). The injection well is at 0 meters and the observation well is at 30 meters. One important trend to notice is that there is a rise in reservoir temperature observed at the CO_2-rich injectant front. As the CO_2-rich injectant moves through the reservoir, the change in concentration created by the arrival of the injectant causes an increase in temperature. This trend is seen in the simulation temperature values at the observation well, Figure 22, when breakthrough occurs on 10/6/2004. The CO_2-rich injectant front is between 10 and 20 meters and produces an increase in temperature between 5 and 15 meters after 1 day (Figure 23a). The CO_2-rich injectant front is between 20 and 35 meters and produces an increase in temperature between 15 and 30 meters after 2 days (Figure 23b). The CO_2-rich injectant front is between 30 and 45 meters and causes an increase

in temperature between 25 and 40 meters after 3 days (Figure 23c). The CO_2-rich injectant front is between 40 and 60 meters and causes an increase in temperature between 35 and 50 meters after 4 days (Figure 23d).

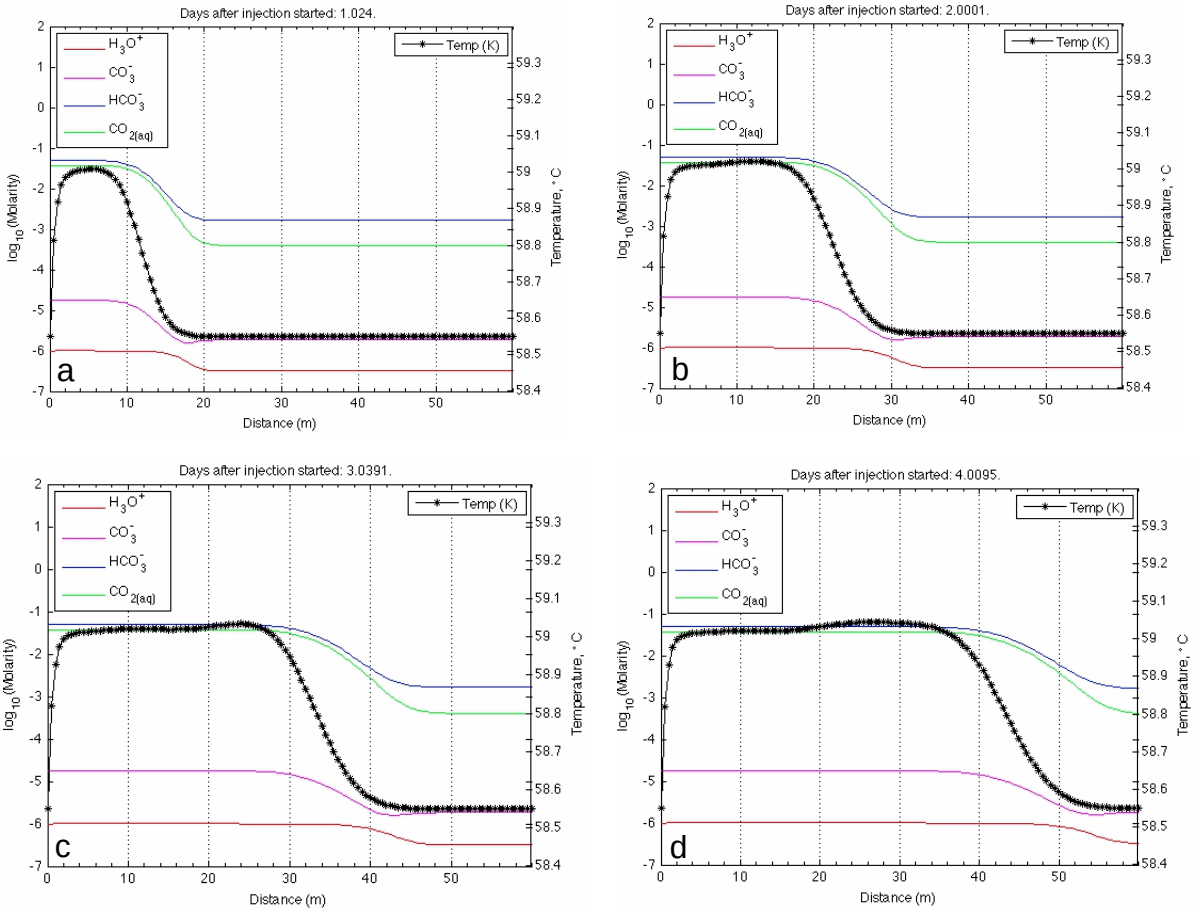

Figure 23. 1-D temperature and concentration profile in time for 0-60 meters of Frio Formation lithology.

Simulation results for the various injection rates of approximately 15, 12, 7.5, and 3.75 meters/day were examined (Figure 24) and normalized (Figure 25). To compare the maximum temperatures of each simulation, the results of each time step for the 12, 7.5 and 3.75 meters/day simulations were multiplied by approximately 0.8, 0.5, and 0.25 so the arrival of the injection front in each simulation would match the 15 meters/day simulation. If an injection rate of 15 meters/day was used, the CO_2-rich injectant would reach the observation well 30 meters away in 2 days, however if an injection rate of 12 meters/day was used, it would reach the observation well in 2.5 days. Thus to compare the increase in temperatures at the observation well when breakthrough occurred after roughly 2 days, the 12 meter/day simulation times are multiplied by 0.8 (2.5 x 0.8 = 2.0) which matches the breakthrough time of the 15 meters/day simulation). The breakthrough curves from various seepage velocities overlap when normalized.

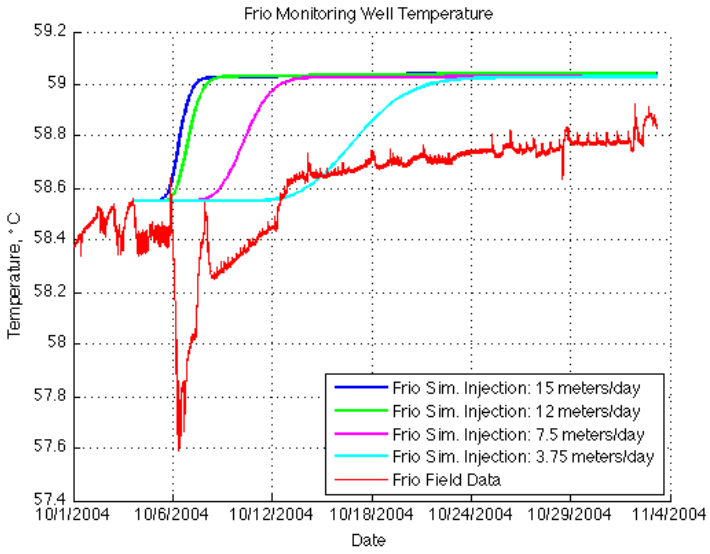

Figure 24. Temperature effects from variations in injection rate.

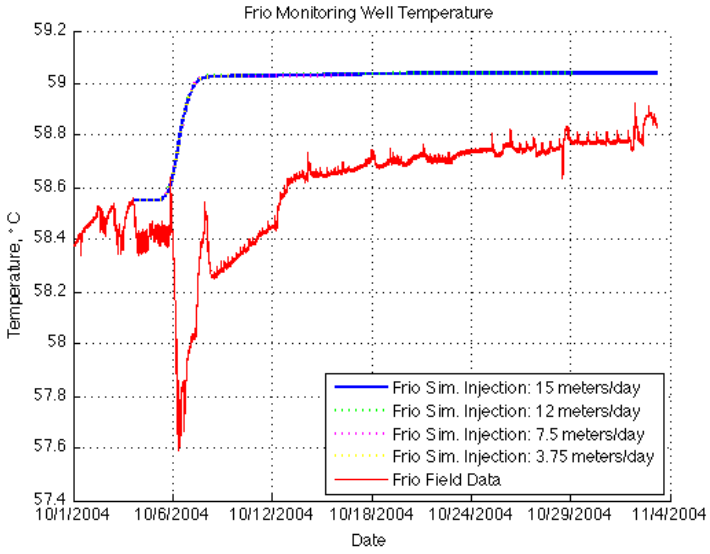

Figure 25. Normalized temperature effects from variations in injection rate.

Simulation results from the various pressures of 148.319 bars, 150.448 bars, and 171.738 bars where compared (Figure 26). It is important to notice that between the simulation with a pressure of 148.319 bars and 150.448 bars, there is little change in the temperature profile. The simulation results from the simulations with various amounts of total inorganic carbon were compared (Figure 27). It is important to notice that as the amount of total inorganic carbon increases in the injectant, the amount of temperature change increases. Likewise, as you decrease the amount of total inorganic carbon in the injectant water, the amount of temperature change decreases. The

simulation results, when the initial temperature is shifted down to 58.4˚C, were also compared (Figure 28). The reason the temperature is shifted down to 58.4˚C is because when injection started, it was on a peak temperature of 58.55˚C, and after a few hours the temperature decreased to an average temperature of 58.4˚C for the next two days. In Figure 28 the simulation with an initial temperature of 58.4˚C provides a better model of the fifth and sixth of October temperatures than simulations with an initial temperature of 58.55˚C. The final simulation temperature for the simulation with an initial temperature of 58.4˚C is also closer to the final Frio field test pilot experiment data temperatures.

Examination of the Frio Test Pilot simulation results show that the temperature increases at the injection front (Figure 22). This is similar to the quartz only simulation results, which also show an increase in temperature at the injection front. Another important fact to notice is that the temperatures at the observation well show little change after the arrival of the CO_2-rich plume and stay at an elevated temperature of approximately 59.05˚C. Further examination of Figure 22 shows little change in temperature between the three simulations with different grid cell spacing. Examination of simulation results also shows little change in the temperature profile between the four selected injection rates of 15, 12, 1.7 and 3.75 meters/day (Figure 25). This shows that the solution is also independent of these relatively fast seepage velocities. This is important because it shows that as the CO_2-rich injectant propagates out from the injection well and slows down, there should be little change in the formation temperature. Finally, examination of simulation results shows that there is little change in the temperature between the minimum Frio Test Pilot Experiment pressure of 148.319 bar and the maximum Frio Test Pilot Experiment pressure of 150.448 bar (Figure 26). This shows that, although the model does not account for pressure changes during injection, this small pressure change does not have an appreciable effect on the temperature profile. One other important aspect to notice in Figure 26 is that if injection occurred for a longer time, and the pressure increase was greater, as in the simulation with a pressure of 171.7380 bars, the temperature profile would change. Thus, for the model to calculate accurately the temperature in longer injection scenarios, a pressure solver would be needed. The overall importance of Figure 22, Figure 25, and Figure 26 is to show that the temperature profile is independent of grid cell spacing, small variations in injection rate, and small variations in pressure.

One important trend to notice is how the amount of total inorganic carbon injected relates to the temperature profile (Figure 27). This is important when determining the maximum amount of CO_2 that can be sequestered in a formation. If there is an observation well sensor or seal that has a maximum temperature threshold, this module helps to predict the amount of CO_2 that can be sequestered without reaching that temperature. Another important trend to notice is that simulation results with an initial temperature of 58.4C are a better representation of the temperatures on

the fourth and fifth of October and is closer to the thermal equilibrium temperature of the Frio Test Pilot Experiment (Figure 28).

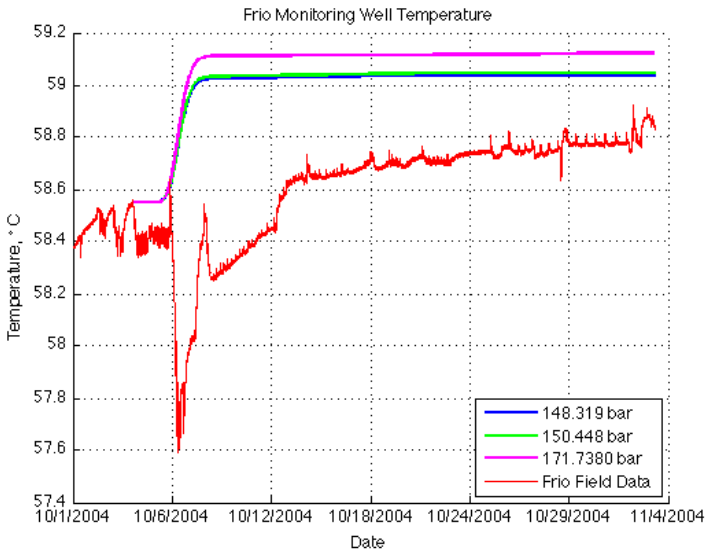

Figure 26. Variations in pressure and its effect on temperature.

Although the temperature module is able to model the temperature increases observed at the Frio Test Pilot Experiment, it is unable to model the initial sudden drop in temperature observed and the gradual temperature increase. Examination of all simulations shows the model is unable to calculate the temperature drop from 58.55˚C to an average of 58.4˚C, which occurs shortly after injection began. This initial drop could result from changes in sampling height, which is shown to result in the small pH drop from 6.7 to 6.5 [1]. Another important temperature drop the model is unable to show is the large temperature drop to 57.6˚C that occurs on October 6.

After the temperature drop of approximately 0.8˚C on October 6 in the field data, the observation well temperature slowly increases and reaches a semi-equilibrium temperature above the initial formation temperature. The simulation shows the temperature increase and equilibrium temperature above the initial temperature. However, a higher equilibrium temperature is reached in the simulation, as opposed in the field. One possible reason for the simulation higher final equilibrium temperature is that, in the field, there is heat transfer in three dimensions, while the simulated heat transfer is only along the x-axis.

Even though the model reaches a higher equilibrium temperature faster than the field data, possibly resulting from modeling in 1D, it shows a reasonable temperature profile, which roughly matches the Frio Test Pilot Experiment. Bielinski et al. [8] used a numerical multi-phase simulation program to study non-isothermal effects resulting from

CO_2 injection. Their model results also showed an increase in temperature with the arrival of CO_2 rich injectant, which is also independent of grid cell spacing (Figure 29).

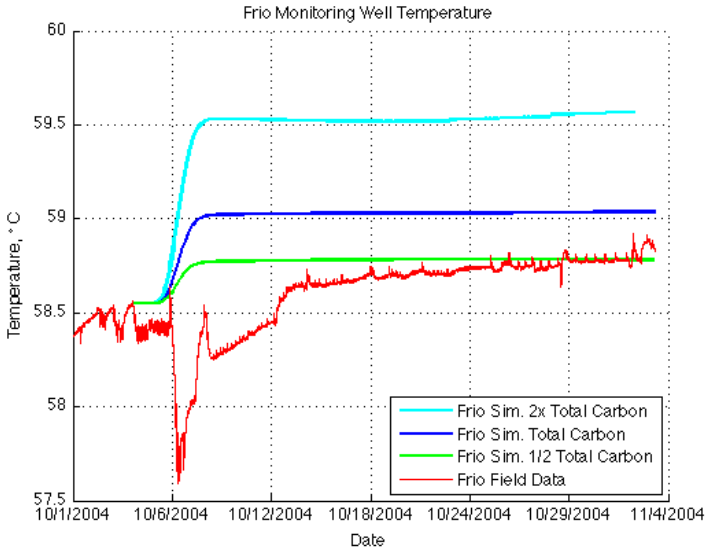

Figure 27. Frio simulations with various total inorganic carbon concentrations.

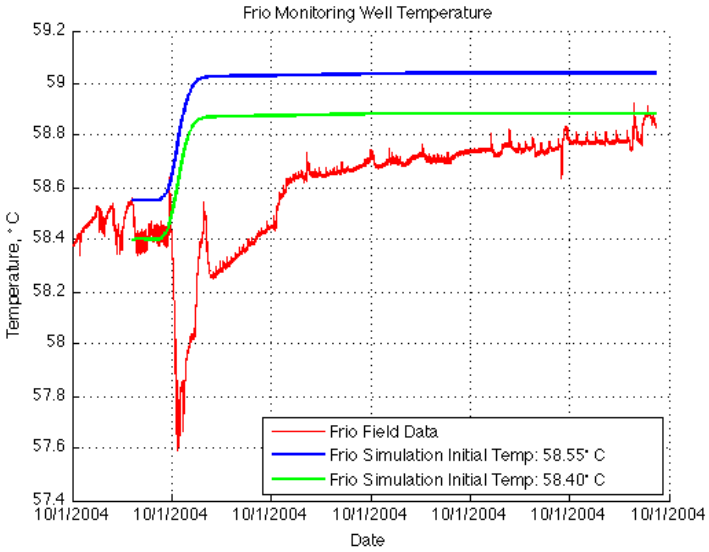

Figure 28. Variations in initial simulation temperature.

The initial temperature, magnitude of temperature increase, and time of temperature increase are all different from the Frio Test Pilot Experiment because of differences in initial temperature, mineralogy, water composition and injection rate. However, it demonstrates that the increase in temperature is independent of the model parameters

and more directly related to changes in total inorganic carbon. Bielinski used their temperature increase to propose that temperature monitoring could be used to detect and monitor CO_2 plumes. The implemented heat transfer module can be used to predict the movement of CO_2-rich waters. When the CO_2-rich water reaches an observation well, it should cause an increase in temperature and the amount of temperature increase is determined by the amount of total inorganic carbon increase from that of the formation to that of the injectant. If an observation well does not have fluid sampling ability, the arrival of the sequestered CO_2 at the well can be determined when the well temperature increases.

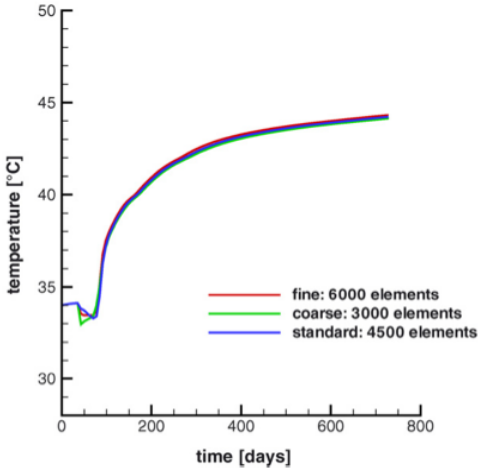

Figure 29. Bielinski et al. (2008) modeled calculated temperatures for a geologic formation in the vicinity of Berlin, Germany.

Eduardo J. Sanchez Peiro is currently developing a parallel mass transport module for his doctoral qualifying examination preparation. This parallel mass transport solver is based upon a parallel large-sparse system solver to compute solute concentrations in parallel on the SDSC TeraGrid/XSEDE system *trestles.sdsu.edu* using the SuperLU distributed solver developed at Lawrence Berkeley National Laboratory.

The evolution of chemical elemental mass depends on mass transfer from diffusive and advective forces as well as the precipitation and dissolution of minerals governed by kinetic reaction rates. The Sim.8 code [9,10], upon which the Web-app is built, solves for elemental mass e_β,

$$\frac{\partial e_\beta}{\partial t} = \sum_{\alpha=1}^{Na} \nu_{\beta\alpha} \left[\phi D_\alpha \nabla^2 c_\alpha - \phi \vec{\nabla} \bullet \left(c_\alpha \vec{u} \right) \right] - \sum_{\gamma=1}^{M} \nu_{\beta\gamma} \rho_\gamma A_\gamma G_\gamma \qquad (8)$$

where the terms in equation (8) are defined as

ϕ	porosity	c	solute concentration	K	equilibrium constant
D	diffusion coefficient	e	chemical elemental mass	Ea	activation energy
u	water flow velocity	G	mineral reaction rate	R	gas constant
ν	reaction stoichiometry	k	reaction rate constant	T	temperature
A	mineral surface area	β	solute atom index	α	aqueous solute species index
		γ	mineral index		
		ρ_γ	mineral solid molar density		

Another doctoral student supported under this award is Jonathan Matthews who developed a poroelasticity rock-mechanics module to simulate rock dilation and compression as a response to changes in pore pressure. The theory of poroelasticity relates the four field properties of pore pressure, fluid gain, stresses and strains in a porous medium. Jonathan has designed a poroelastic pore pressure module that calculates the stresses induced by the injection of CO_2 into sandstone. In a one-dimensional case, the pore pressure decouples from the stresses, fluid gain, and strains, and the induced stresses are a linear function of the pore pressure. The decoupled pressure follows a diffusive process that is a function of the fluid sources and the poroelastic properties of the rocks. The resultant mean stresses in the rocks of each cell in the model were computed. The calculated stresses can be used to estimate the occurrence and behavior of rock fractures. Oda's permeability tensor is employed as a method for calculating the impact of fractures on permeability. The pore pressure module was used to approximate formation pressure during injection of CO_2 rich water into the Oligocene Frio Formation along the Texas Gulf Coast, with simulation parameters derived from the Frio Test Pilot Experiment. Simulation results were compared to bottom-hole pressure data obtained from an observation well 30 meters away from the injection well, during a 35-day injection phase.

This discretized pore pressure diffusion code computes the resultant mean stresses in rock when subjected to CO_2 injection. The calculated stresses are used to investigate the occurrence and propagation of rock fractures in sandstone. The pressure diffusion code implements the following non-homogeneous diffusion equation,

$$\frac{\partial p}{\partial t} - c\nabla^2 p = -\frac{\alpha}{S}\frac{dg}{dt} + \frac{Q}{S} \tag{9}$$

However, in the case of an irrotational displacement field, where the boundary conditions ε, σ_{kk}, and p vanish at an infinite boundary, the integrating constant *g(t)* is identically zero, so the equation simplifies to

$$\frac{\partial p}{\partial t} - c\nabla^2 p = \frac{Q}{S} \tag{10}$$

In order to model fractures, the internal stresses incurred by the saturated rock matrix must first be calculated. There are two types of computational models for calculating these stresses: *direct* models, which track the formation and evolution of many micro-cracks, and *indirect* models, which determine effects by constitutive relations and use a

continuum approximation to describe the rock [11]. While direct models such as Potyondy and Cundall's bonded particle model can provide much detailed information on the evolution of stresses and cracks, they may prove computationally prohibitive at geologic time and length scales. However, they may prove useful in modeling fractures that are local in time and space to the injection of CO_2.

Poroelasticity is a macroscopic theory of the coupling of changes in stress and changes in fluid pressure in fluid-saturated isotropic porous media. The theory explains phenomena first studied in the fields of geomechanics, hydrogeology, and petroleum engineering in a unified way. J. Geertsma coined the term *poroelasticity* and noted, "the mathematical description of the macroscopic theory of poroelasticity is similar to that used in the theory of thermoelasticity." [12]

Four field quantities are described by poroelasticity: an applied stress tensor σ_{ij}, strain tensor ε_{ij}, fluid gain ζ, and pressure p, with the subscripts i and j representing coordinate directions relative to a *representative elementary volume* (REV). The stress tensor σ is a second rank tensor, whose components σ_{ij} are defined relative to a REV as a force per unit area acting in the i -direction on a face normal to the j -direction. Stress components are commonly divided into two types: *normal stresses*, σ_{ii}, where the force is parallel to the normal of the face it acts upon, and *shearing stresses*, σ_{ij} for $i \neq j$, where the force is perpendicular to the normal of the face as shown in Figure 30.

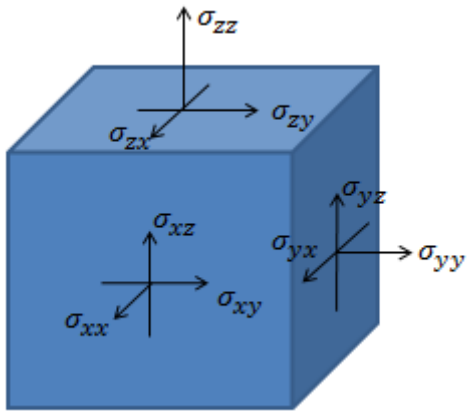

Figure 30. Stresses on a representative elementary volume (REV).

The strain tensor ε is second rank tensor describing the local deformation of a material relative to a reference state. If u, v, and w represent the displacements in the x, y, and z directions for a given point, then strain is defined with the spatial derivatives of these displacements:

$$
\begin{aligned}
\epsilon_{xx} &= \frac{\partial u}{\partial x} \\
\epsilon_{yy} &= \frac{\partial v}{\partial y} \\
\epsilon_{zz} &= \frac{\partial w}{\partial z} \\
\epsilon_{xy} &= \frac{1}{2}\left(\frac{\partial u}{\partial y} + \frac{\partial v}{\partial x}\right) \\
\epsilon_{xz} &= \frac{1}{2}\left(\frac{\partial u}{\partial z} + \frac{\partial w}{\partial x}\right) \\
\epsilon_{xy} &= \frac{1}{2}\left(\frac{\partial v}{\partial z} + \frac{\partial w}{\partial y}\right)
\end{aligned}
\tag{11}
$$

As with stress, there are tensile strains and shear strains as shown in Figure 31 and Figure 32.

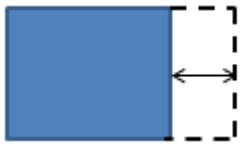

Figure 31. Tensile Strain.

Figure 32. Shear Strain.

The incremental fluid gain ζ is the amount of fluid gained or lost by a REV relative to a reference value. This variable has units of volume, and is essentially a proxy for the fluid mass gained or lost in an REV. The formal definition of fluid gain is determined by first looking at the change in fluid mass content of the REV $\delta m_f = m_f - m_{f_0}$ where m_f is the fluid mass content per unit reference volume and m_{f_0} is the fluid mass content in a fixed reference state. If ρ_{f_0} is the fluid density for the reference state, the fluid gain is defined by

$$
\zeta = \frac{\delta m_f}{\rho_{f_0}} \tag{12}
$$

The pore pressure *p* is the pressure of the fluid occupying the pore space in the porous medium. The *mean stress* is defined by

$$\sigma = \frac{\sigma_{11} + \sigma_{22} + \sigma_{33}}{3} = \frac{1}{3}\sigma_{kk} \tag{13}$$

where the Einstein summation notation is adopted whereby if a subscript is repeated in one term of a formula (e.g. *kk* subscript for σ) it is summed over all indices. In this context, it will correspond to summation over the three coordinate directions. The individual stress components σ_{ij} are dependent on the choice of coordinate axes, however the *first stress invariant*, $I_1 = \sigma_{kk}$ is independent of the choice of axes [13]. It follows, therefore, that the mean stress is also independent of the chosen axes. The volumetric strain is defined as

$$\epsilon = \frac{\delta V}{V_0} = \epsilon_{kk} \tag{14}$$

ε_{kk} is an invariant of the strain tensor in a manner similar to mean stress, so it is also independent of the choice of axes. The simplest set of linear constitutive relations can be framed in terms of these two invariants along with the incremental fluid gain and pore pressure. Under an isotropic stress conditions, the following two constitutive equations govern the four field quantities:

$$\begin{aligned} \epsilon &= \frac{1}{K}\sigma + \frac{1}{H}p \\ \zeta &= \frac{1}{H}\sigma + \frac{1}{R}p \end{aligned} \tag{15}$$

Note that in constitutive equations, each quantity is considered to be relative to a reference state. As such, when a quantity such as pressure is held constant, the expressions *p=0* and $\delta p = 0$ are considered equivalent [12]. The coefficient $\frac{1}{K}$ is the compressibility of the material under *drained conditions*. Drained conditions are conditions of constant pore pressure (*p=0*) as would occur if fluid was allowed to freely drain out through the pores at constant pressure while a confining pressure is applied to the solid material. This coefficient is the reciprocal of *K*, the drained bulk modulus. The coefficient $\frac{1}{H}$ describes how much the bulk material volume changes due to changes in pore pressure, while holding confining stress constant. By energy considerations, this is the same coefficient that describes the amount of incremental fluid gain due to changes in confining stress under constant pore pressure [12]. This explains why the coefficient matrix associated with equations (15) is symmetric. The coefficient $\frac{1}{R}$ is a storage coefficient describing how much fluid is gained per unit reference volume under constant confining stress. This coefficient is designated

$$S_\sigma \equiv \frac{1}{R} \tag{16}$$

and is referred to as the *unconstrained specific storage* coefficient. The term *unconstrained* refers to the fact that under constant confining stress, the volumetric strain may not be constant. A similar uniaxial specific storage coefficient is used in the uniaxial strain case discussed in this final report. Two more coefficients commonly used to describe the poroelastic properties of a material are *Skempton's coefficient B* and *Biot's coefficient* α, both of which are related to the constants already established in equations (15). Skempton's coefficient describes the effect on pressure induced by an increase in compressive stress under undrained ($\zeta = 0$) conditions. It shows the pressure reaction to an instantaneously applied compressive load before flow allows the fluid to escape the reference volume, or the pressure induced by a compressive load in a sealed sample. Given that compressive stress has negative magnitude, Skempton's coefficient is defined as

$$B \equiv -\left.\frac{\delta p}{\delta \sigma}\right|_{\zeta=0} = \frac{R}{H} \tag{17}$$

Biot's coefficient relates the incremental fluid gain to the volumetric strain under constant pore pressure,

$$\alpha \equiv \left.\frac{\delta \zeta}{\delta \epsilon}\right|_{p=0} = \frac{K}{H} \tag{18}$$

Before generalizing to the non-isometric stress case, some parameters from classical elasticity are needed. Young's Modulus *E* relates the tensile stress required to produce a unit strain in a material,

$$\sigma_{ii} = E\epsilon_{ii} \tag{19}$$

In an isotropic material undergoing tensile stress, the strain along the axis of tension will be accompanied by a contraction in the transverse directions. Poisson's Ratio, ν, is the negative of the ratio of the transverse strain to the axial strain, that is,

$$\nu = -\frac{\epsilon_{yy}}{\epsilon_{xx}} = -\frac{\epsilon_{zz}}{\epsilon_{xx}} \tag{20}$$

for a tensile stress applied along the *x*-axis. In the theory of poroelasticity, ν refers to the *drained* Poisson's ratio which measures this parameter under drained (*p=0*) conditions. In the undrained case (ζ =0), the parameter is referred to as ν_u. The shear modulus *B* satisfies the relation

$$G = \frac{E}{2(1+\nu)} \tag{21}$$

and measures the amount of shear stress required to produce a unit change in shear angle, γ_{ij}, which is in turn twice the shear stress.

$$\sigma_{ij} = G\gamma_{ij} = 2G\epsilon_{ij} \tag{22}$$

Finally, Young's modulus is related to *K* by

$$E = 3(1-2\nu)K \tag{23}$$

In many cases, stresses are not isotropic, but for any stress state, there exists a set of mutually perpendicular axes for which all shear stresses are zero. These are known as the principal axes of the stress state. These axes are always oriented in the directions of the maximum tensile stress, the minimum tensile stress and a third axis perpendicular to both. In the isotropic case, any choice of mutually perpendicular axes can be principal axes. We can then generalize the first constitutive equation (15) by breaking it into the three principal stress components. The system then becomes

$$\begin{aligned}
\epsilon_{xx} &= \frac{\sigma_{xx}}{E} - \frac{\nu}{E}\sigma_{yy} - \frac{\nu}{E}\sigma_{zz} + \frac{P}{3H} \\
\epsilon_{yy} &= -\frac{\nu}{E}\sigma_{xx} + \frac{\sigma_{yy}}{E} - \frac{\nu}{E}\sigma_{yy} + \frac{P}{3H} \\
\epsilon_{zz} &= -\frac{\nu}{E}\sigma_{xx} - \frac{\nu}{E}\sigma_{yy} + \frac{\sigma_{zz}}{E} + \frac{P}{3H} \\
\zeta &= \frac{1}{H}\frac{\sigma_{xx}+\sigma_{yy}+\sigma_{zz}}{3} + \frac{P}{R}
\end{aligned} \tag{24}$$

which reduces to equations (15) when $\sigma_{xx} = \sigma_{yy} = \sigma_{zz}$.

Darcy's law is a constitutive equation relating fluid flux, $\vec{q}$ to the gradient of fluid pressure in porous materials. In its standard form, Darcy's law is expressed as

$$\vec{q} = -\frac{k}{\mu}\overrightarrow{\nabla p} \tag{25}$$

where *k* is the permeability of the material and μ is the viscosity of the fluid. The permeability has units of area, which are usually expressed in terms of the Darcy [D] or milli-Darcy [mD]. One Darcy is approximately $10^{-12} m^2$. Darcy's original model was for one-dimensional fluid flows through soil and included permeability as a constant. However, when Darcy's Law is expanded to three dimensions, it becomes apparent that permeability may vary by direction. Consider a thick metal plate with disconnected holes drilled into its face. The permeability of the plate will be significant perpendicular to the plate as fluid can pass through the holes, but it will be zero for any direction within the plane of the plate, as there are no channels traveling along the plane of the plate. Permeability is therefore not always isotropic (the same in all directions.) It must be represented as a second order tensor in anisotropic cases and is denoted k_{ij}.

The flux $\vec{q}$ is not the actual velocity of a particle of fluid through the pore space, but an average velocity taken over the volume of both the pore space and the solid matrix. Darcy's law is a continuum approximation of the rather discontinuous behavior of fluid flowing through pore channels. Flow is zero in the space occupied by the solid matrix and non-zero in the pore spaces. We can define an average *seepage velocity* by dividing the flux by the fraction of total volume occupied by pore space.

This fraction, called the *porosity* and denoted by ϕ, is defined as the pore volume in a reference volume divided by the total volume of the reference volume. Note that porosity, ϕ, is dimensionless, whereas permeability, *k*, has units of area. Specimens of the same porosity can have different permeabilities, depending on the geometry of the pore space. We can now define the average seepage velocity as

$$\vec{v} = \frac{1}{\phi}\vec{q} \tag{26}$$

Biot and Willis expressed the incremental fluid gain by

$$\zeta = -\phi\vec{\nabla}\cdot(\vec{U}_f - \vec{U}_s) \tag{27}$$

where $\vec{U}_f$ and $\vec{U}_s$ are the average displacements of the fluid and solid respectively. The seepage velocity can be considered as the difference between the velocities of the fluid and the solid matrix as seepage velocity is the average velocity of the fluid relative to the solid matrix. Seepage velocity can then be written relative to the time derivatives of the displacements

$$\vec{v} = \dot{\vec{U}}_f - \dot{\vec{U}}_s = \frac{1}{\phi}\vec{q} \tag{28}$$

Combining equation (28) and the time derivative of equation (27) yields

$$\frac{\partial\zeta}{\partial t} = -\vec{\nabla}\cdot\vec{q} \tag{29}$$

This equation can be generalized to include an external source, *Q(t)*, of fluid added to the REV,

$$\frac{\partial\zeta}{\partial t} = -\vec{\nabla}\cdot\vec{q} + Q(t) \tag{30}$$

In this equation, *Q* is expressed in terms of fluid volume per unit reference volume per unit time. If Darcy's law (25) is substituted into the above equation, a time dependent diffusion equation results

$$\frac{\partial\zeta}{\partial t} = \frac{k}{\mu}\nabla^2 p + Q(t) \tag{31}$$

In the case of the one dimensional Sym.8 simulation, a symmetry argument can be made that the two horizontal axes constitute principal coordinates for the stress state if gravity is neglected. The assumption that the reservoir is surrounded by rigid cap rock and that the domain is infinite such that the stresses are equalized in the radial dimension, we have the uniaxial strain case $\epsilon_{yy} = \epsilon_{zz} = 0, \quad \sigma_{xx} = 0$. Substituting these uniaxial strain conditions into the first two equations of (24) and summing them gives

$$\begin{aligned} 0 &= \frac{(1-\nu)}{E}(\sigma_{yy} + \sigma_{zz}) + \frac{2}{3H} p = \frac{(1-\nu)}{E}\sigma_{kk} + \frac{2}{3H} p \\ \sigma_{kk} &= -\frac{2E}{3(1-\nu)H} \end{aligned} \tag{32}$$

Substituting (23) for *E*, gives

$$\sigma_{kk} = \frac{2(1-2\nu)K}{(1-\nu)H} p = \frac{2(1-2\nu)}{(1-\nu)} \alpha p = 4\eta p \tag{33}$$

where $\eta = \frac{1-2\nu}{2(1-\nu)}\alpha$. Detournay and Cheng [14] refer to this constant as the *poroelastic stress coefficient*. Substituting $\sigma_{kk}/3$ for σ in equation (15) gives

$$\zeta = \frac{\sigma_{kk}}{3H} + \frac{1}{R} p = \left(-\frac{4\eta}{3H} + \frac{1}{R} \right) p = Sp \tag{34}$$

where *S* is the *uniaxial specific storage coefficient*. Following some algebra using some of the relations among poroelastic constants, the formula for *S* shown in equation (49) is developed as outlined in [12]. The stress field is then decoupled from the pore pressure field in this case. Substituting equation (34) into equation (31) gives the following uniaxial pore pressure diffusion equation

$$\frac{\partial p}{\partial t} = \frac{k}{\mu S} \nabla^2 p + \frac{Q(t)}{S} = c \nabla^2 p + \frac{Q(t)}{S} \tag{35}$$

where $c = \frac{k}{\mu S}$. The parameter *c* is known as the *hydraulic diffusivity*.

In Sym.8's one dimensional simulator, the reservoir is modeled as a 1cm by 1cm parallelepiped of user-specified length, *L*, divided into *M* evenly sized cells according to the number of cells specified in the input file. The horizontal coordinates can be represented by values $x_1 \ldots x_n$. The x_i s are defined by setting

$$\Delta x = \frac{L}{M - 1} \tag{36}$$

where

$$x_i = \Delta x(i - \frac{1}{2}) \tag{37}$$

for all *i*'s from 1 to *M*. The time step is set dynamically according to the dynamics of the system at a given time step. For discretization of time, the values at a particular time step *n* are denoted with a superscript. The n[th] time step is labeled $\Delta t^n = t^{n+1} - t^n$. A pressure value is calculated for each cell for each time step. In one dimension, the pressure diffusion equation(35) becomes

$$\frac{\partial p}{\partial t} = c\frac{\partial^2 p}{\partial x^2} + \frac{Q(t)}{S} \tag{38}$$

This equation is discretized using central difference on the spatial second derivative and backward difference on the time derivative yields the following discrete equation for the central cell's pressure

$$\frac{p_i^{n+1} - p_i^n}{dt^n} = c\frac{p_{i-1}^{n+1} - 2p_i^{n+1} + p_{i-1}^{n+1}}{(\Delta x)^2} + \frac{Q^{n+1}}{S} \tag{39}$$

Parameters $r^n = c\frac{\Delta t^n}{(\Delta x)^2}$ and $\tilde{Q}^n = \frac{\Delta t^n Q^n}{S}$ are defined and the *n+1* time step pressure terms are isolated on the right-hand side. Equation (39) becomes

$$p_i^n + \tilde{Q}^{n+1} = -rp_{i-1}^{n+1} + (2r+1)p_i^{n+1} - rp_{i+1}^{n+1} \tag{40}$$

Dirichlet boundary conditions are used at the left and right boundaries,

$$\begin{aligned} p_0^{n+1} &= p_0^n = \ldots = p_0^0 \\ p_M^{n+1} &= p_M^n = \ldots = p_M^0 \end{aligned} \tag{41}$$

This yields the matrix equation,

$$\begin{bmatrix} p_1^n + \tilde{Q}_1^{n+1} \\ p_2^n + \tilde{Q}_2^{n+1} \\ \vdots \\ p_{M-1}^n + \tilde{Q}_{M-1}^{n+1} \\ p_M^n \end{bmatrix} = \begin{bmatrix} (r+1) & -r & & & & & & \\ -r & (2r+1) & -r & & & & & \\ & \ddots & \ddots & \ddots & & & & \\ & & -r & 2r+1 & -r & & & \\ & & & \ddots & \ddots & \ddots & & \\ & & & & -r & (2r+1) & -r & \\ & & & & & 0 & 1 & \end{bmatrix} \begin{bmatrix} p_1^{n+1} \\ p_2^{n+1} \\ \vdots \\ p_{N-1}^{n+1} \\ p_N^{n+1} \end{bmatrix} \tag{42}$$

This tridiagonal system is solved in Sym.8 using the LAPACK tridiagonal solver routine *dgtsv*.

It is clear from Darcy's law (25) and equation (26), that fluid flows are heavily dependent on both the permeability and porosity of the rock. Local fractures in a rock can affect both properties, though the impact to permeability is likely to be much more significant. Porosity changes may occur if disconnected pores become connected upon

the initiation or growth of a crack [15]. Otherwise, fractures are not likely to affect porosity significantly unless they cause the rock to expand or contract on a macro scale, because the same mass of solid material will still be contained within the same volume if there is no macroscopic expansion or contraction. Therefore, most gains in pore space created by cracks will occur at the expense of contractions in the remaining pore space. Permeability, however, is heavily dependent on the geometry of the pore space. Fractures create channels that facilitate fluid flow, so they increase permeability in the plane of the crack. The overall effect of fractures can be estimated using a technique by Oda [16].

The concept of a permeability tensor and its role in Darcy's law are best suited to a porous medium such as a sandstone or soil. Oda developed a model to express the ability of a fluid to flow through a cracked or jointed rock by determining a porous medium equivalent permeability. Not all networks of fractures or joints can be appropriately modeled with such a porous medium equivalent approach. These include cases where there are few cracks or cracks to not extend far into the medium. In order to use such a model for a given volume of material, there must be a sufficient number of cracks within that volume that are well interconnected. Conversely, the reference volume should not be so large that heterogeneity in the rock makes such a porous medium equivalent model inaccurate. An appropriately sized reference volume must be large enough that the porous medium equivalent model is appropriate, but small enough to encompass a relatively homogeneous region of the rock mass. Such a reference volume is known as a REV (representative elementary volume).

Oda's model gives a porous medium equivalent permeability based on the density, orientations, and dimensions of the cracks. Oda's model was developed under an assumption of penny-shaped cracks, but it could be adapted for other shapes if necessary. Under Oda's model, a crack is characterized by its normal vector, diameter and hydraulic aperture. The hydraulic aperture is related to the geometric aperture of the crack, but is defined by the relationship between pressure gradient and flow within the crack rather than its exact dimensions. The normal vector is represented by $\vec{n}$ and aperture *t*. For consistency with Oda's formulas, the diameter is represented in this paper by *r*, not *d*. A probability density function $E(\vec{n},r,t)$ describes the probability of a crack with normal vector $\vec{n}$, diameter *r*, and aperture *t* within an infinitesimal solid angle $d\Omega$ about $\vec{n}$, diameter between *r* and *r*+*dr* and aperture between *t* to *t*+*dt*. A crack density is defined as the number of cracks per unit volume ρ. Stemming from an idealized laminar flow between parallel plates and the volume of the penny shaped cracks, a so-called *cubic law* relates fluid flow to the pressure gradient. Using this cubic law, Oda developed the following theoretical formula for permeability, which involves integrating over a hemispherical solid angle Ω and the range of possible crack diameters and apertures,

$$k_{ij} = \lambda(P_{kk}\delta_{ij} - P_{ij}) \tag{43}$$

Here, the repeated subscript *kk* indicates summation over all coordinate indices, and δ_{ij} is the Kronecker delta operator. The *crack tensor*, P_{ij}, is defined as

$$P_{ij} = \frac{\pi\rho}{4}\int_0^{r_m}\int_0^{t_m}\int_\Omega r^2 t^3 n_i n_j E(\vec{n},r,t)\,d\Omega\,dt\,dr \tag{44}$$

In equation (43), λ is a non-dimensional coefficient between 0 and $\frac{1}{12}$ that essentially quantifies the impact of connectivity among joints on the permeability. For infinitely large crack diameters or crack densities, $\lambda = \frac{1}{12}$. Oda [16] states that most rocks are cracked to a large extent and that $\lambda = \frac{1}{12}$ can be used in most cases. This simplifying assumption was used for the simulations we conducted.

If we consider a two-dimensional profile of fractures, the model simplifies somewhat. In the two-dimensional case, the normal vector can be fully described by a single angle relative to a reference direction. The categorization of a two dimensional crack is shown in Figure 33 where the fracture diameter is simply the fracture length *r=l*. In two dimensions, the crack density then becomes the number of cracks per unit area rather than volume. In equation (44) the differential solid angle simplifies to a differential arc.

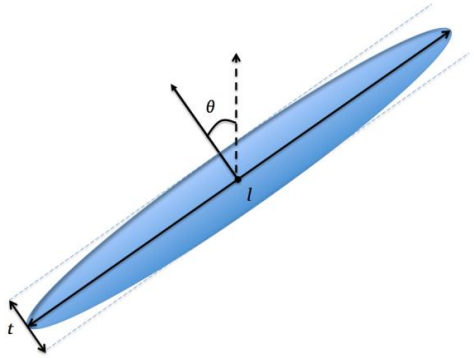

Figure 33. Example Fracture Parameters in Two Dimensions.

Given a set of fracture geometries, a discretized form of equation (44) can be used in order to calculate the fracture-induced permeability of a rock. In two dimensions, looking at the cracks in an $L \times L$ square REV that is *T* thick, the integral can be converted to the following summations in equations (45).

$$\begin{aligned} P_{11} &= 1/TL^2 \sum^{m(V)} Tr^{(k)} (t^{(k)})^3 cos^2\phi^{(k)} \\ P_{12} = P_{21} &= 1/TL^2 \sum^{m(V)} Tr^{(k)} (t^{(k)})^3 cos\phi^{(k)} sin\phi^{(k)} \\ P_{22} &= 1/TL^2 \sum^{m(V)} Tr^{(k)} (t^{(k)})^3 sin^2\phi^{(k)} \end{aligned} \tag{45}$$

Since permeability is a tensor, it can be rotated into alternative reference frames without changing its physical interpretation. In the special case of isotropic permeability with constant *k*, the tensor is diagonal with value *k* at each position of the diagonal, regardless of the axes' orientation. For any symmetric tensor, such as the permeability tensor, there is an orientation such that the tensor becomes diagonal. As with the stress tensor, these are known as the *principal axes* of the permeability tensor.

An important practical consideration about the computed permeability is the relationship between a pressure gradient in direction $\vec{p}$ and the flow that it would induce in that direction. This value is the constant of permeability in the one-dimensional Darcy's Law. Oda states that this directional permeability is defined by [16]

$$K^{(\vec{p})} = k_{ij} p_i p_j \tag{46}$$

This model neglects the possibility that the matrix between rock fractures is permeable in any way. In fact, Oda [17] tested the theoretical permeability model by validating it against granite from a mine in Sweden. Granite is sufficiently crystalline that such an impermeable matrix assumption is reasonable. For sandstone and shale, such impermeability is not accurate, but Oda's model can be used to estimate just the incremental permeability due to the fractures themselves, separate from any permeability of the matrix. This can then be added to the permeability tensor of the matrix.

The discrete crack tensor formula in equations (45), can estimate the permeability due to a given set of fractures. Because it is not feasible to directly quantify the actual fractures in a particular CO_2 injection site, randomly generated fractures are a model that can be used as a proxy for the actual fracture profile of a rock. In modeling applications, the defining parameters of the random distribution of cracks would be determined by the in situ state of the rock, or perhaps by a fracture nucleation or growth model. These will be the focus of future research. To demonstrate the technique of simulating and calculating the permeability of a rock from its fracture profile, rather simple models for generating the diameter, aperture, and orientation of the fractures were used in the examples that follow. Though the positions of individual cracks within the REV are not used in Oda's model, the random crack center locations were simulated in order to make the visual representations of the randomly fractured rocks shown in Figure 34 and Figure 35. A 1m x 1m square, two-dimensional REV was used as the basis for permeability simulations. For each randomly generated fracture, the *x* and *y* coordinates of the fracture centers were generated uniformly between 0 and 1, and the apertures were generated uniformly between 0 and an input maximum aperture. The orientation angles were generated both uniformly between 0 and π, as well with a truncated normal distribution for comparison purposes. For CO_2 sequestration modeling, the distributions are replaced by distributions derived from the results of fracture nucleation and growth models. From the random orientation angles, we calculated the components of the normal vector of each crack. The total number of cracks were

modeled from a Poisson distributed random variable with the expected number of cracks as the input parameter. Figure 34 and Figure 35 show example simulations with approximately 50 cracks each. The truncated normal distribution used here has mean orientation of 0.8 radians measured counterclockwise between the crack's normal vector and the vertical axis. From the random fracture data, the crack tensor is calculated using equations (45) and the permeability tensor using equation (43). For example, the random fracture profile shown in Figure 35 produces the crack tensor,

$$P = \begin{bmatrix} 0.1286 & 0.0157 \\ 0.0157 & 0.0840 \end{bmatrix} \times 10^{-7}\, m^2 \tag{47}$$

From this crack tensor, the associated permeability tensor was calculated using equation (46),

$$k = \begin{bmatrix} 0.0700 & -0.0131 \\ -0.0131 & 0.1072 \end{bmatrix} \times 10^{-8}\, m^2 \tag{48}$$

With the permeability tensor *k*, the directional permeabilities in every direction were calculated and plotted using a polar plot as shown in Figure 36. In this polar plot, it is apparent that the permeability is largely isotropic in the *xy*-plane (circular in the polar plot), but there is slightly less resistance to flow in the vertical direction.

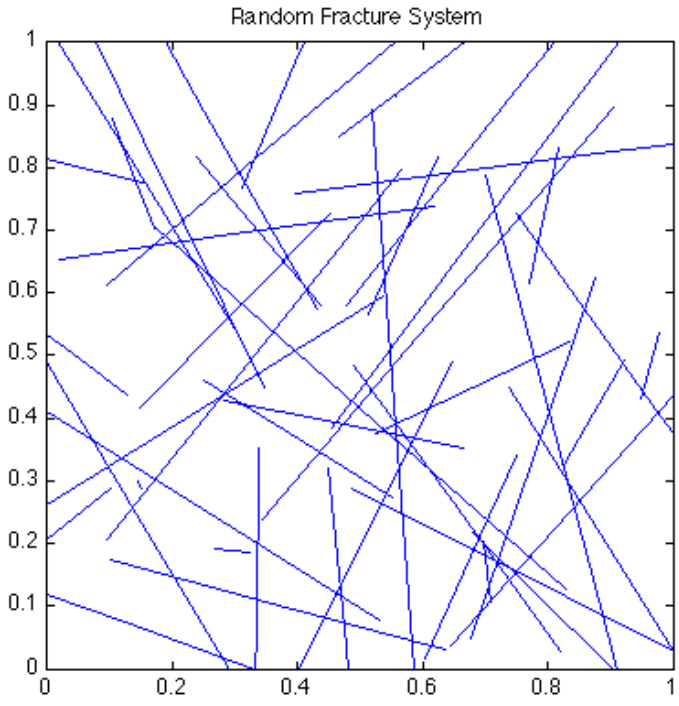

Figure 34. 50 Random fractures with uniform orientation distribution.

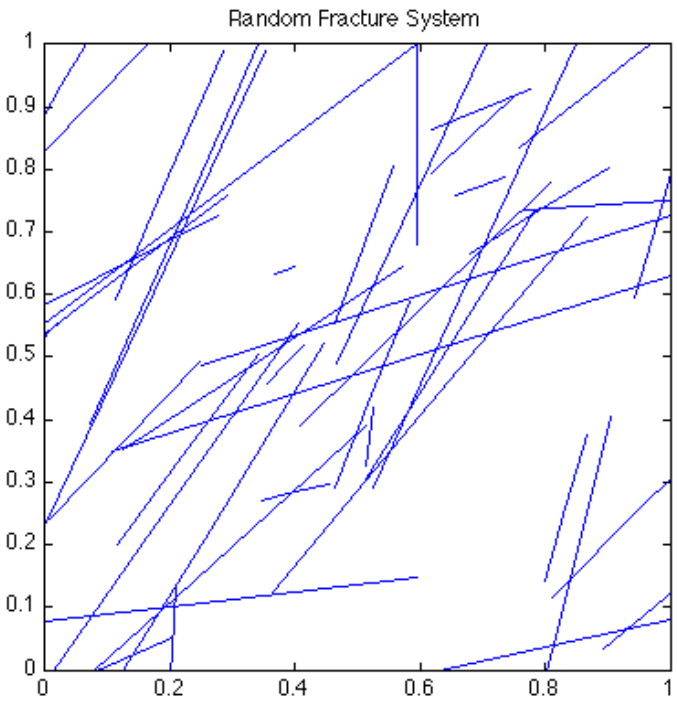

Figure 35. 50 Random fractures with truncated normal orientation distribution.

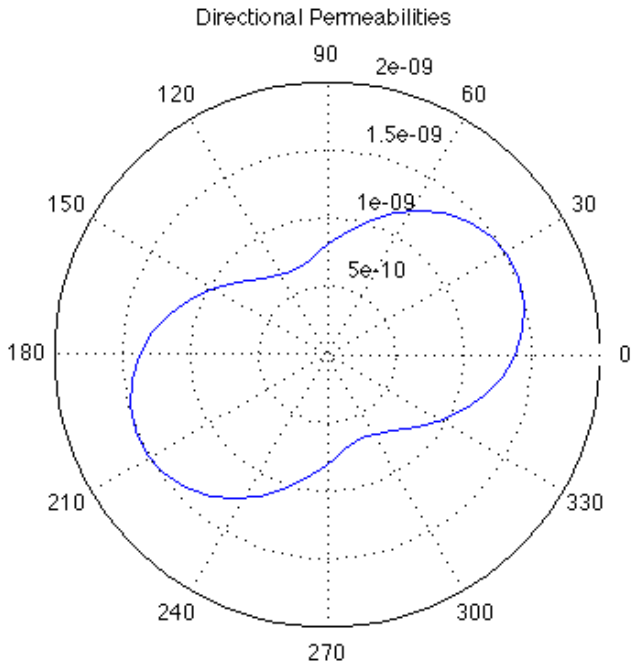

Figure 36. Directional permeabilities (m^2) arising from 50 uniformly oriented cracks.

The same method was used to calculate the directional permeabilities of the cracks shown in Figure 35, yielding the directional permeability plot shown in Figure 37. Clearly, the flow in this scenario favors one direction more strongly than all others.

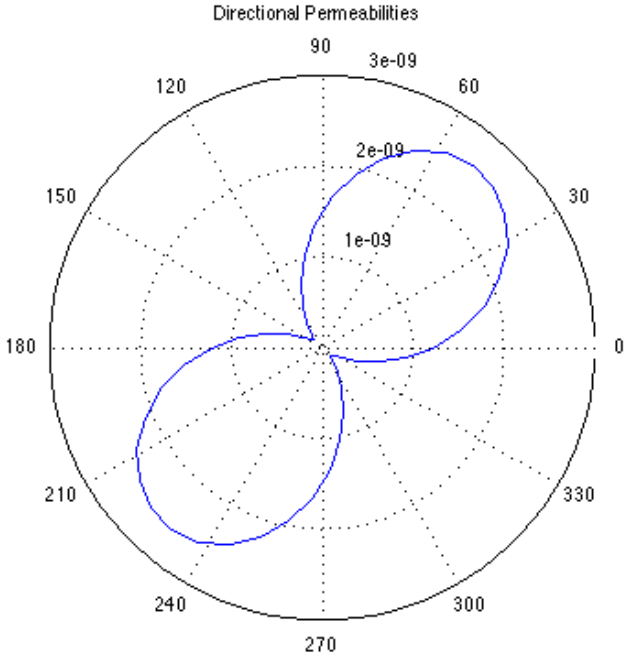

Figure 37. Directional permeabilities (m^2) arising from 50 normally-distributed orientation cracks.

In 2004, a pilot test was conducted in sandstones of the Frio formation, east of Houston Texas. The pilot was conducted to test the viability of using geologic formations other than reservoirs from which hydrocarbons had been extracted for the storage and sequestration of CO_2. During the test, about 16,000 tons of CO_2 were injected into a sandstone formation 5,050 feet underground over a period of ten days. An existing well 100 feet from the injection site was used to monitor the pressure, temperature and chemical composition. Lawrence Livermore National Laboratories conducted simulations using their TOUGH2 multiphase flow simulation model [18]. An input file for Sym.8 was developed from the TOUGH2 input file used for the Lawrence Livermore simulations. Carpenter and Spencer [19] examined the pore compressibility of Frio sandstone, but did not include information on the other poroelastic moduli. Detournay and Chang [14] and Wang [12] have compiled tables of poroelastic properties of various types of sandstones and other rock species with Wang's table being the more comprehensive. Boise sandstone has the highest porosity of the sandstone species compiled by Wang, with $\phi = 0.26$. This is most comparable to the Frio formation porosity of $\phi = 0.31$, so unknown poroelastic constants for Frio sandstone were

substituted using Boise sandstone data. The uniaxial specific storage coefficient can be calculated in terms of the Biot modulus *M*, the drained Poisson's ratio ν, and the undrained Poisson's ratio ν_u,

$$S = \frac{(1-\nu_u)(1-2\nu)}{M(1-\nu)(1-2\nu_u)} \tag{49}$$

Both Poisson's ratios are included in Wang's table, but *M* is not. *M* can be expressed in terms of Skempton's coefficient *B*, the undrained bulk modulus K_u, and the Biot-Willis coefficient α,

$$M = \frac{BK_u}{\alpha} \tag{50}$$

We can then calculate the uniaxial specific storage by combining equations (49) and (50),

$$S = \frac{\alpha(1-\nu_u)(1-2\nu)}{BK_u(1-\nu)(1-2\nu_u)}$$

Figure 38 shows the evolution of pressures of the model run with grid spacing of 1.0m at an injection pressure of 250 bar. The initial pressure profile shows a sharp pressure change between the injection boundary and the rest of the domain. The pressure diffusion calculation then causes the pressure to increase across the domain until it approaches a straight line between the two boundaries. This corresponds to the steady flux assumption used in prior analyses. Figure 39 shows the increment of mean stress relative to the *in situ* state of the reservoir at various time steps. This is simply a linear function of the pressures shown in Figure 38. Therefore, under this model, the stress level will be strictly increased during CO_2 injection unless some additional conditions occur, such as confining stress changes or fracturing. The pressure evolution model was run at grid spacings of 0.25m, 0.50m and 1.00m, respectively, with an injection pressure of 150.0 bar. Figure 40 shows the pressure values plotted versus time at 30m from the injection site. The figure shows that the three runs are converging to the same solution. The plot also shows that the pressure profile is approaching the steady state pressure of 149.86 bar asymptotically. Figure 41 shows the same pressure profile at 30m focused on a small time frame centered around the one-year mark of the simulation. This plot clearly demonstrates the convergence of the more refined solutions. The induced pressure gradients produce flow away from the injection site as expected. Using a permeability of 800 mD, the flow rate was shown to be consistent with the Frio experiment. Figure 42 shows the simulated concentration profiles of hydrogen ions, aqueous CO_2, bicarbonate ions, and carbonate ions, respectively, just after injection was initiated. Figure 43 shows the acidic front of the CO_2 plume reaching the 30m mark between 3-4 days after the start of injection. The observation well was located in the Frio experiment at this distance. In the Frio test case, the front reached the observation well after three days, which is consistent with this simulation. Figure 44

shows the simulated concentration profiles toward the end of the Frio experiment and the diffusive front traveling well beyond the observation well by the end of the experiment.

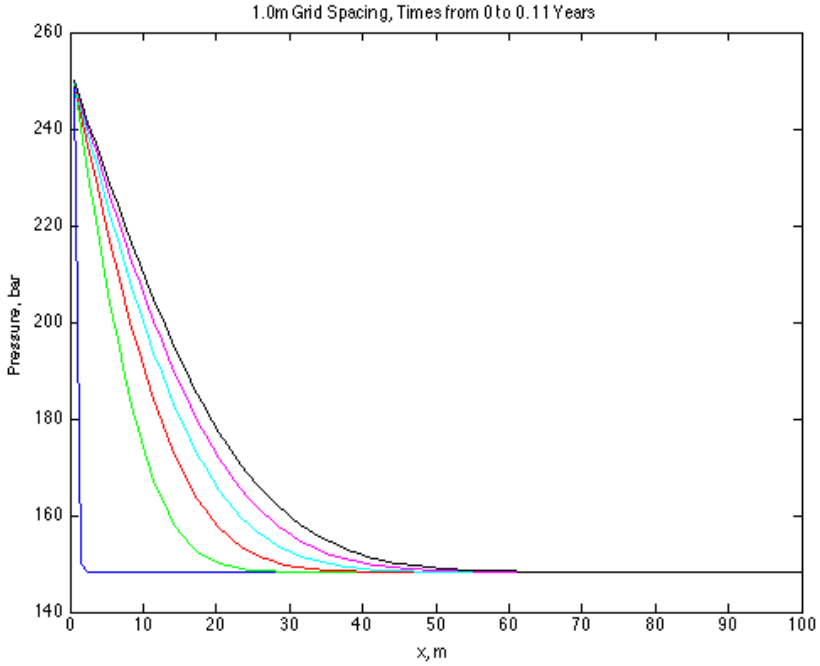

Figure 38. Pressure profiles for the 1.0m grid spacing at six uniformly spaced times.

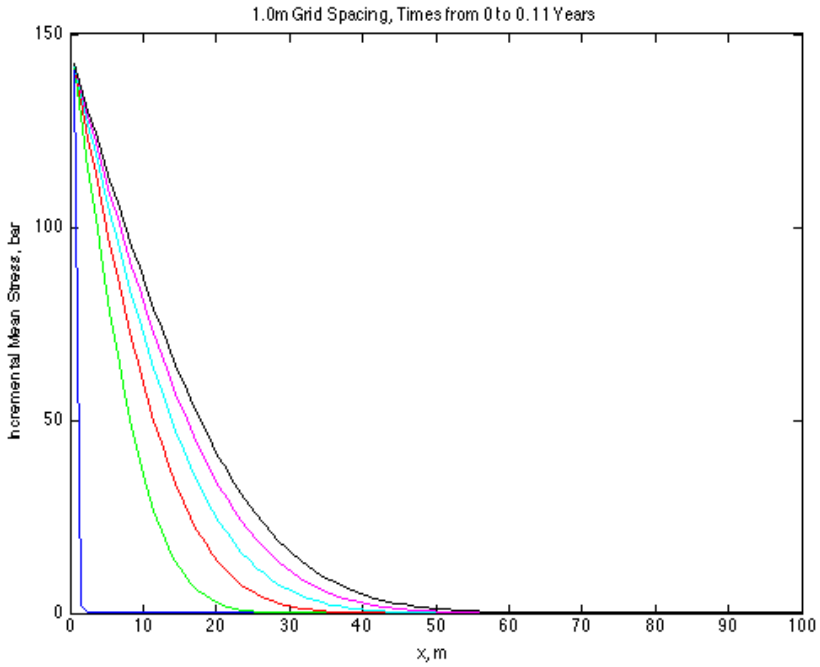

Figure 39. Pressure profiles for the 1.0m grid spacing at six uniformly spaced times.

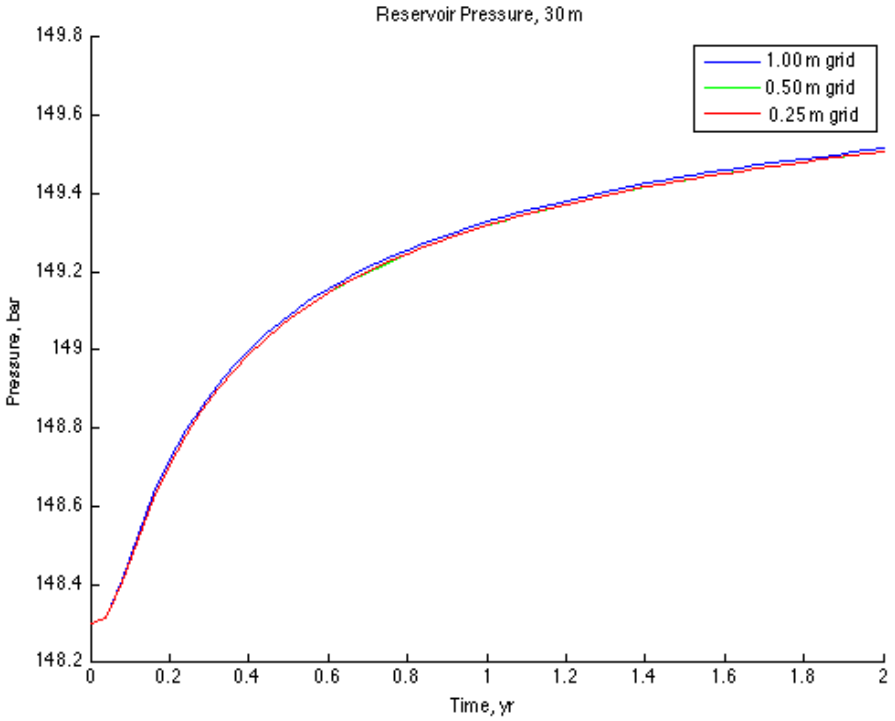

Figure 40. Comparison of pressure profiles at 30m by grid spacing.

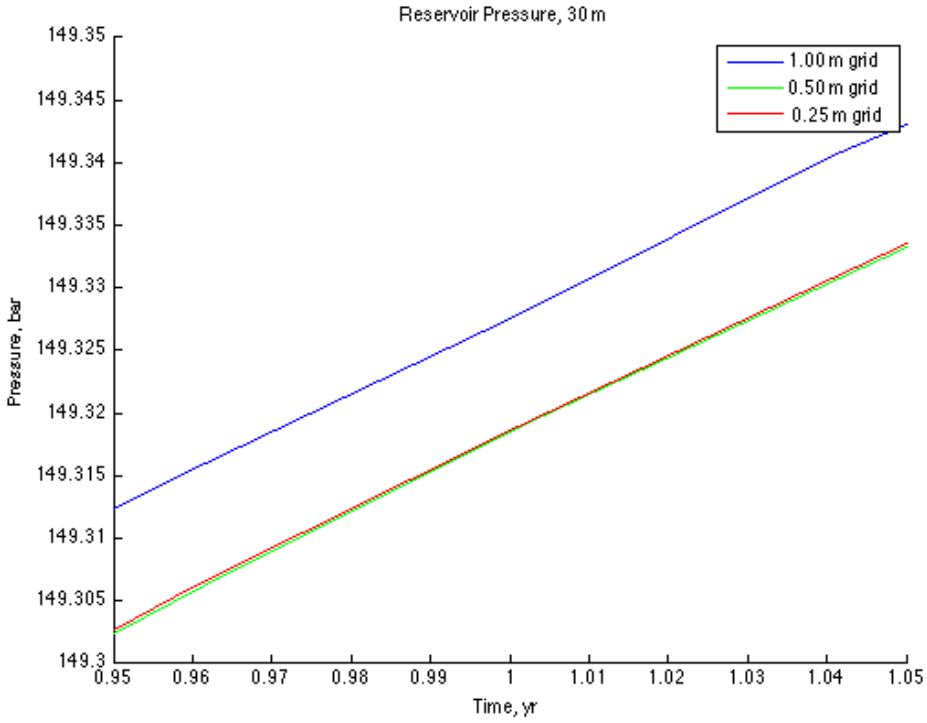

Figure 41. Comparison of pressure profiles at 30m by grid spacing.

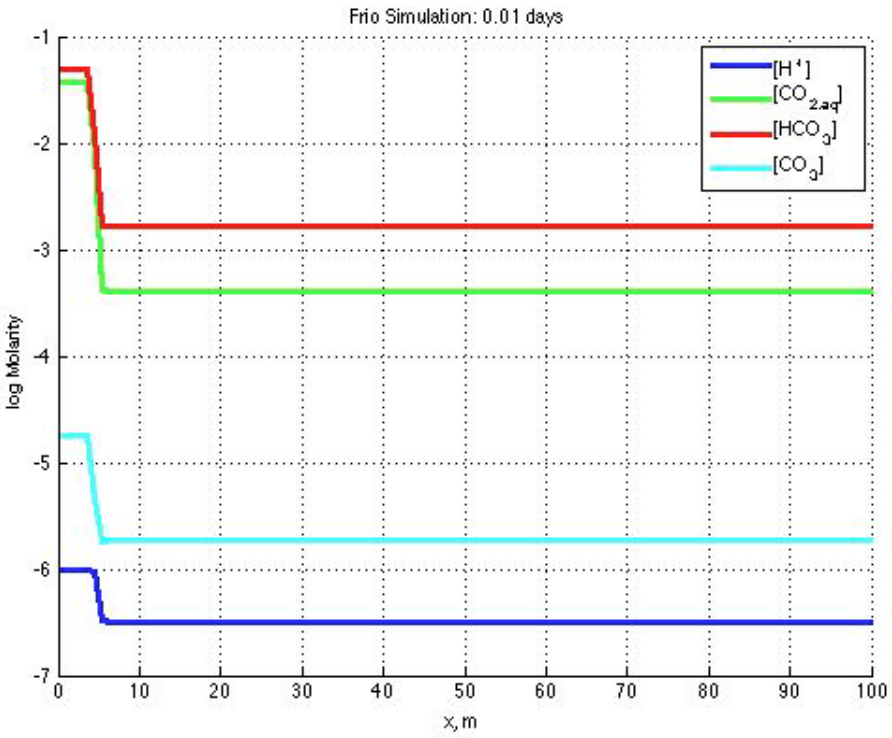

Figure 42. Solute concentrations at the onset of the Frio test, 1.0m grid spacing.

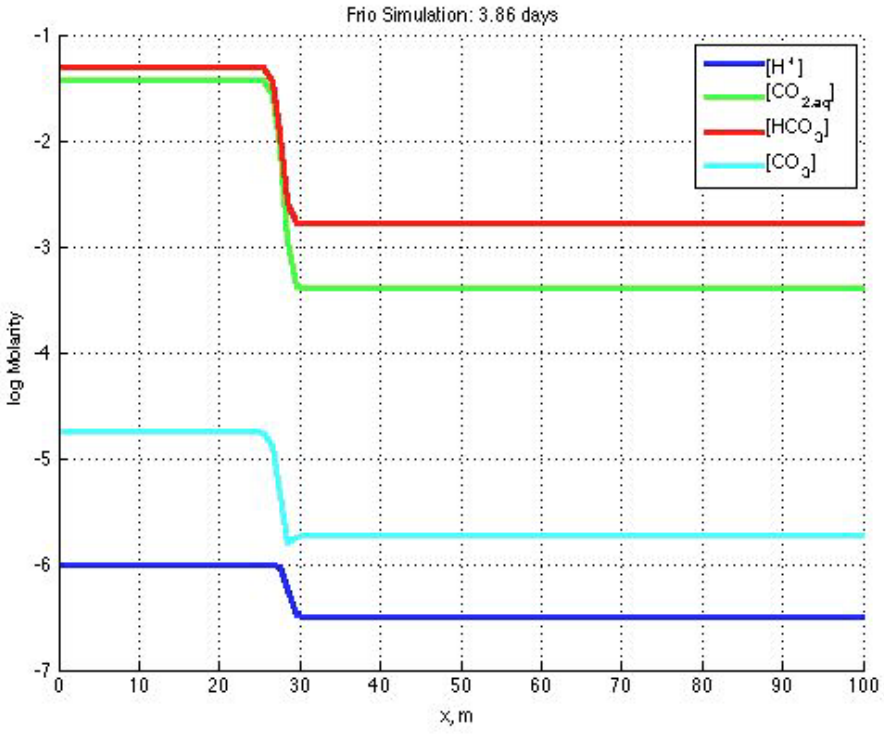

Figure 43. Solute concentrations at the time of the CO_2 plume reaching 30m for the Frio test, 1.0m grid spacing.

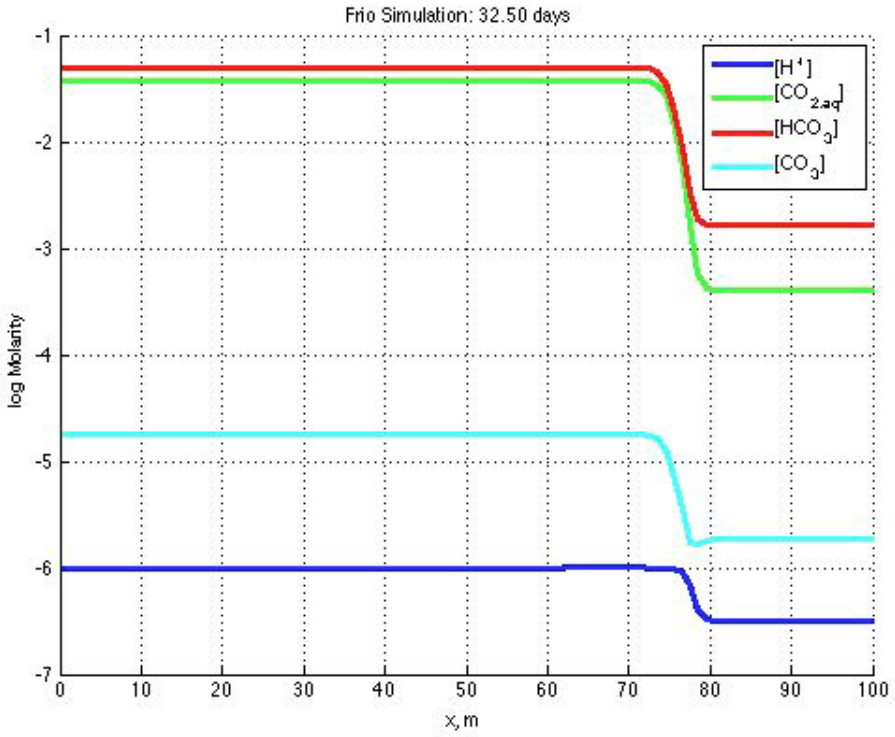

Figure 44. Solute concentrations at termination of the Frio test, 1.0m grid spacing.

Conclusion

We presented a paper and two posters at the 10th Annual Conference on Carbon Capture and Sequestration held May 2-5, 2011, in Pittsburgh, Pennsylvania [2]. Our paper addressed the utilization of Sym.8 to study the effects of varying CO_2 concentrations and seepage velocities on porosity and permeability. One of the main questions is how CO_2 will affect the subsurface geology. To address this question, porosity, permeability, and mineralogical changes must be measured around the injection well as CO_2 is being sequestered. We showed how the use of Sim.8 is an advantageous tool that can be used to model these changes before site injection commences. With the Web interface we developed for Sym.8, we showed how it is possible to quickly and easily model a range of subsurface lithologies and their response to a range of injection solutions, thus limiting costly and time intensive field experiments. Our paper addressed the use of Sim.8 to better understand the effects of CO_2 concentration and seepage velocities on porosity and permeability. 1D horizontal simulations were run with CO_2 aqueous concentrations ranging from 0.1M to 1.0M being injected for 5 years at seepage velocities of 100, 300 and 500 [cc/(cm^2 yr)]/φ through a homogenous sandstone formation. All simulations showed an overall increase in porosity and permeability due to the dissolution of calcite, initially present at a volume fraction of 5%. Increasing the CO_2 concentration and seepage velocity had no effect on the maximum porosity and permeability values. However, increasing CO_2

concentration and seepage velocities resulted in slight decreases in porosity and permeability behind the injection front. This can be attributed to calcite precipitation behind the injection front. Simulations with no initial calcite show higher final CO_2 aqueous concentrations leading to the conclusion that calcite precipitation behind the injection front provides mineral trapping of CO_2. Thus, if the intent of CO_2 injection is to maximize porosity and permeability, low seepages velocities around 100 [cc/(cm^2 yr)]/φ should be used to limit calcite precipitation behind the injection front. However if the intent of CO_2 injection is to maximize CO_2 storage as mineralized calcite, injection of water with high CO_2 concentrations at seepage velocities around 500 [cc/(cm^2 yr)]/φ should be used.

Our conference poster addressed the incorporation of new Web technology to expand the accessibility and flexibility of reaction-transport-modeling software. The advancements of mobile technology allow Internet access in more places than ever before. However, there has always been a tradeoff between mobility and speed. The computational power to run most geologic modeling software requires it be done on desktop or server computers, thus limiting mobility. Our poster showed how emerging new Website technologies can be incorporated with complex CCUS modeling software. This incorporation bridges the gap between personal Internet devices and powerful servers. The poster presented the novel AJAX-based Web application we developed through this award, that allows a user to define, run, and view CCUS simulations on any computer with Internet access and a standard Web browser. Computationally intensive simulations are carried out on a remote server, allowing complex simulations to be run, regardless of the user's local browser device speed. Another advantage of such a design is that the user can run and view simulations on a range of computers without having to save and manage CCS configuration or output files. This allows a user to modify, quickly, resident and injectant water compositions, lithological characteristics, and simulation parameters all from a Web browser. Several CO_2 sequestration scenarios were modeled using the Web interface to Sym.8. One scenario modeled 1D horizontal injection of CO_2-rich water with CO_2 aqueous concentrations ranging from 0.1M to 1.0M being injected for 5 years at seepage velocities of 100, 300 and 500 [cc/(cm^2 yr)]/φ through a homogenous sandstone formation. The Web application allows easy configuration and viewing of results, which show the transport of tracer ions along the injection front and dissolution-precipitation of minerals. Decreases in porosity and permeability were observed behind the injection front, which correlates with a precipitation of calcite. Another scenario modeled was 1D vertical diffusion of CO_2 through sandstone and a shale cap rock. Simulations modeling 5 years of vertical diffusion showed no CO_2 leakage through the cap rock and little change in porosity and permeability. The usefulness of the Web interface to RTM software developed through this award is not only in modeling CO_2 sequestration, but also in the accessibility and

flexibility that is central in its construction, and has proved to be a useful tool to use in an organized university course on carbon capture and sequestration.

One of our stated goals was to foster further development of the Computational Science program at San Diego State University. This grant provided ongoing support for three graduate students: Christopher Binter (MS Geological Sciences), Eduardo J. Sanchez Peiro (PhD Computational Science), and Jonathan L. Matthews (PhD Computational Science). Christopher Binter successfully defended his geological sciences master's thesis, entitled *Implementation of the Helgeson-Kirkham-Flowers Model to Study Reservoir Temperature Evolution during CO_2 Injection*, on October 30, 2012. The thesis defense was recorded and is available for viewing online via URL: http://www.geology.sdsu.edu/people/students/theses/fall2012/christopher_binter.html

One of the many deliverables resulting from this grant was a software module that computes 1D transient and steady state heat transfer to study the temperature effects of CO_2 injection. Temperature and cell specific thermal diffusivity, heat conductivity, heat capacity and density are calculated using the model. Thermal energy generation is determined using solute specific heat capacity and enthalpy values calculated using the Helgeson-Kirkham-Flowers model. Frio Test Pilot Experiment simulation lithology and water compositions were configured similar to the Frio Test Pilot Experiment. The simulation results show a similar temperature profile to what was measured by field observations and reported as well data. In both the simulation and field data, the arrival of the CO_2-rich injectant resulted in an increase in temperature. The simulator was unable to show the initial drop in temperature seen in the field data. However, both the simulation and field data temperatures roughly reach the same equilibrium temperature, higher than when injection began. Furthermore, our temperature model is able to show that small changes in pressure and advection will have little effect on the temperature profile. This is important because pressure and advection rate changes will occur as the CO_2-rich plume migrates outward from the injection well. The amount of CO_2 injected appears to be one control on the magnitude of temperature change. This is important when trying to determine the maximum amount of CO_2 that can be sequestered without damaging well bore instruments or seal integrity. With this heat transfer module, *what if* scenarios can be simulated using WebSimC, our developed Web interface to Sim.8, to determine the temperature increase resulting from CO_2-rich water injection. This allows for estimations of temperature changes possible in the formation before injection begins. If it is determined that well bore instruments or seals can only withstand certain maximum temperature, appropriate total inorganic carbon concentrations can be selected. CO_2 plumes could possibly be monitored using temperature signals resulting from increases in temperature caused by the arrival of the CO_2-rich injectant. This would provide observation wells without fluid sampling facilities a way to track the movement of the plume, purely though temperature changes observed at the well.

To model solute transport correctly, it appears that a higher permeability value for the resident sandstone would need to be used. The current calculated permeability for the Frio test case is 11.3 milli-Darcy, but data compiled by Wang [12] show that similarly porous sandstone varieties such as Boise sandstone can have a permeability at least as high as 800 mD. This order of magnitude appears likely to be large enough to account for the discrepancy in solute arrival times for the Frio test case versus the model. In order to determine whether fractures are occurring, the threshold at which fractures begin to occur must be determined. Eckert and Nygaard [20] have studied the critical pore pressures that will lead to induced shear and tensile fractures in injection reservoirs. This is an important step in modeling rock fractures as this is the threshold above which the behavior of the rock ceases to be elastic, and fracture dynamics must be considered. Once the stresses exceed the critical levels, the initiation and evolution of micro and macro cracks must be examined. Gutierrez [21] has used an approach using randomized fracture geometries to estimate the effects of fracturing on the permeability and elastic properties of rock. Since fracture occurrence is heavily dependent on the unknown micro-structure of the reservoir, the results of such a randomized approach can be used in concert with Monte-Carlo simulations to yield a range of possible outcomes for a proposed sequestration scheme. This paper and other simulations of CO_2 sequestration assume straight, horizontally-oriented reservoirs. Geologic features such as anticlines cause variations in the slope of the reservoir over the horizontal region. Eckert and Nygaard [20] are also examining the impact of such features. In particular, they are examining the impact that the location of the injection site within the crests limbs and valleys of these geological features has on the stresses experienced in the reservoir. We implemented a simplified model that assumes irrotational, uniaxial strains, which reduces the system to a spatial derivative in terms of pressure and a linear relationship between pressure and mean stress. A more general case would explicitly consider the fluid gain and strain terms. Such a case can be analyzed using a finite element technique [12,14]. Similar studies may be done for fluid flows in other types of subsurface reservoir rocks such as shales and cap rock species like halite and dolomite. Further modeling may be done of the pressure evolution at the boundaries of these species. Once the subsurface stresses have been determined, the formation and evolution of cracks must be examined. Further, the effects of these cracks on porosity, permeability and surface area must be accounted for in the model. The cementation site of a borehole well used for CO_2 sequestration has strong potential to be a point of failure for containment of CO_2 due to its in-homogeneity with the surrounding rock and reservoir. Cary [22] is researching the long-term integrity of well seals. Research into this area includes the carbonation and corrosion impact of exposure to CO_2 in wells, the self-sealing nature of both the cement and steel in the well casing, leakage along the cement-casing interface, and geomechanical modeling of wellbore stresses. Dvorkin [23] has investigated the non-homogeneity of porosity in the rock by dividing a studied cell into sub-volumes and randomizing the porosities and lithologies within a specified range. Since microscopic differences can create differences in porosity and therefore local pressure levels, this may be an effective way to model the peak pressures and resultant stresses within a given discretized volume. A non-homogeneous permeability profile is generated if the Oda permeability tensor model is used independently for each finite volume cell in the model. When modeling

crack formation, it will be important to distinguish between a rock's propensity to crack when saturated with fluid versus when it is saturated with gaseous CO_2. Labuz has been investigating the drained and undrained fracturing of Berea sandstone using a technique measuring acoustic emissions caused by the formation of microcracks. The experiments seem to indicate that for similar compressive loading, more microcracks form in the drained than undrained specimens [24].

References

[1] Y. Kharaka et al., "Gas-water-rock interactions in Frio Formation following CO2 injection: Implications for the storage of greenhouse gases in sedimentary basins," *Geology*, vol. 34, no. 7, pp. 577-580, July 2006.

[2] C. Binter, C. Paolini, A. J. Park, and J. E. Castillo, "Utilization of Reaction-Transport Modeling Software to Study the Effects of Reservoir Temperature and Seepage Velocity on the Sweep Diffusion Front Displacement Formed after CO2-Rich Water Injection," in *Tenth Annual Conference on Carbon Capture and Sequestration*, Pittsburgh, Pennsylvania, May 2-5, 2011.

[3] C. Paolini, A. J. Park, C. Binter, and J. E. Castillo, "An investigation of the variation in the sweep and diffusion front displacement as a function of reservoir temperature and seepage velocity with implications in CO2 sequestration," in *47th AIAA/ASME/SAE/ASEE Joint Propulsion Conference & Exhibit and the 9th Annual International Energy Conversion Engineering Conference*, San Diego, California, 31 Jul - 3 Aug 2011.

[4] W. H. Press, *Numerical Recipes: The Art of Scientific Computing*, 3rd ed.: Cambridge University Press, 2007.

[5] J. W. Demmel, S. C. Eisenstat, J. R. Gilbert, X. S. Li, and J. W. H. Liu, "A supernodal approach to sparse partial pivoting," *SIAM J. Matrix Analysis and Applications*, vol. 20, no. 3, pp. 720-755, 1999.

[6] X. S. Li and J. W. Demmel, "SuperLU Dist: A scalable distributed-memory sparse direct solver for unsymmetric linear systems," *ACM Trans. Mathematical Software*, vol. 29, no. 2, pp. 110-140, 2003.

[7] T. Xu, Y. K. Kharaka, C. Doughty, B. M. Freifeld, and T. M. Daley, "Reactive transport modeling to study changes in water chemistry induced by CO2 injection at the Frio-1 brine pilot," *Chemical Geology*, vol. 271, pp. 153-164 , 2010.

[8] A. Bielinski, A. Kopp, H. Schutt, and H. Class, "Monitoring of CO2 plumes during storage in geological formations using temperature signals: Numerical investigation," *International Journal of Greenhouse Gas Control*, vol. 2, no. 3, pp. 319-328, 2008.

[9] A. J. Park. (April, 2011) Sym.8: General Water-rock Interaction and Reactive-Transport Modeling. Software.

[10] A. J. Park, "Water-Rock Interaction and Reactive Transport Modeling Using Elemental Mass-Balance and Explicitly Coupled Iteration Methods: I. the Methodology," Sienna Geodynamics and Consulting, Inc., Bloomfield, Il, 2009.

[11] D. O. Potyondy and P. A. Cundall, "A bonded-particle model for rock," *International journal of rock mechanics and mining sciences*, vol. 41, no. 8, pp. 1329-1364, 2004.

[12] H. Wang, *Theory of linear poroelasticity: with applications to geomechanics and hydrogeology*.: Princeton University Press, 2000.

[13] J. M. Gere, *Mechanics of Materials*, 5th ed.: Brooks Cole, 2001.

[14] E. Detournay and A. H. D. Cheng, *Fundamentals of poroelasticity, Comprehensive Rock Engineering*.: Pergamon, 1993, vol. Vol 2: Analysis and Design Methods, Eds. Brown, ET, Fairhurst, CH and Hoek, E.

[15] J. Jaeger, N. Cook, R. Zimmerman, and R. Zimmerman, *Fundamentals of rock mechanics*.: Wiley-Blackwell, 2007.

[16] M. Oda, "Permeability tensor for discontinuous rock masses," *Geotechnique*, vol. 35, no. 4, 1985.

[17] M. Oda, Y. Hatsuyama, and Y. Ohnishi, "Numerical experiments on permeability tensor and its application to jointed granite at Stripa mine, Sweden," *Journal of Geophysical Research*, vol. 92, no. B8, pp. 8037--8048, 1987.

[18] S. Hovorka, "Frio Brine Pilot: The first US sequestration test," *Southwest Hydrology*, vol. 8, no. 5, 2009.

[19] C. Carpenter and G. Spencer, *Measurements of compressibility of consolidated oil-bearing sandstones*.: United States Department of the Interior, Bureau of Mines, 1940, vol. 3540.

[20] J. Eckert and R. Nygaard, "Numerical modeling of geomechanical processes

related to CO2 injection within generic reservoirs," in *National Energy Technology Laboratory Carbon Storage R&D Project Review Meeting*, Pittsburgh , PA, 2012.

[21] M. Gutierrez, "Training and Research on Probabilistic Hydro-Thermo-Mechanical (HTM) Modeling of CO2 Geological Sequestration (GS) in Fractured Porous Rocks," in *National Energy Technology Laboratory Carbon Storage R&D Project Review Meeting*, Pittsburgh, PA, 2012.

[22] B. Carey, "CO2-Water-Rock Interactions and the Integrity of Hydrodynamic Seals," in *National Energy Technology Laboratory Carbon Storage R&D Project Review Meeting*, Pittsburgh, PA, 2012.

[23] J. Dvorkin, "Rock Physics of Geologic Carbon Sequestration/Storage," in *National Energy Technology Laboratory Carbon Storage R&D Project Review Meeting*, Pittsburgh, PA, 2012.

[24] J. Labuz, "Geomechanical simulation of fluid-driven fracture," in *National Energy Technology Laboratory Carbon Storage R&D Project Review Meeting*, Pittsburgh, PA, 2012.